The First VERA Astrometry Catalog

VERA collaboration, Tomoya Hirota,[1,2,*] Takumi Nagayama,[3]
Mareki Honma,[3,4,5] Yuuki Adachi,[3] Ross A. Burns,[1] James O. Chibueze,[6,7]
Yoon Kyung Choi,[8] Kazuya Hachisuka,[3] Kazuhiro Hada,[3,4]
Yoshiaki Hagiwara,[9] Shota Hamada,[10] Toshihiro Handa,[10,11]
Mao Hashimoto,[12] Ken Hirano,[3] Yushi Hirata,[10] Takanori Ichikawa,[10]
Hiroshi Imai [10,11,13] Daichi Inenaga,[12] Toshio Ishikawa,[3] Takaaki Jike,[3,4]
Osamu Kameya,[3,4] Daichi Kaseda,[10] Jeong Sook Kim,[14] Jungha Kim,[2]
Mi Kyoung Kim,[3] Hideyuki Kobayashi,[1,2] Yusuke Kono,[1,2]
Tomoharu Kurayama,[15] Masako Matsuno,[10] Atsushi Morita,[10]
Kazuhito Motogi,[16] Takeru Murase,[10] Akiharu Nakagawa,[10,11]
Hiroyuki Nakanishi,[10,11] Kotaro Niinuma,[16] Junya Nishi,[12] Chung Sik Oh,[14]
Toshihiro Omodaka,[10] Miyako Oyadomari,[13] Tomoaki Oyama,[3]
Daisuke Sakai,[3] Nobuyuki Sakai,[14] Satoko Sawada-Satoh,[16]
Katsunori M. Shibata,[1,2] Makoto Shizugami,[1,17] Jumpei Sudo,[10]
Koichiro Sugiyama,[18] Kazuyoshi Sunada,[3,4] Syunsaku Suzuki,[1]
Ken Takahashi,[3] Yoshiaki Tamura,[3,4] Fumie Tazaki,[3] Yuji Ueno,[3] Yuri Uno,[10]
Riku Urago,[10] Koji Wada,[10] Yuan Wei Wu,[19] Kazuyoshi Yamashita,[3]
Yuto Yamashita,[10] Aya Yamauchi,[3] and Akito Yuda[10]

[1]Mizusawa VLBI Observatory, National Astronomical Observatory of Japan, 2-21-1 Osawa, Mitaka, Tokyo 181-8588, Japan
[2]Department of Astronomical Sciences, SOKENDAI (The Graduate University for Advanced Studies), 2-21-1 Osawa, Mitaka, Tokyo 181-8588, Japan
[3]Mizusawa VLBI Observatory, National Astronomical Observatory of Japan, 2-12 Hoshigaoka, Mizusawa-ku, Oshu, Iwate 023-0861, Japan
[4]Department of Astronomical Sciences, SOKENDAI (The Graduate University for Advanced Studies), 2-12 Hoshigaoka, Mizusawa-ku, Oshu, Iwate 023-0861, Japan
[5]Department of Astronomy, Graduate School of Science, The University of Tokyo, 7-3-1 Hongo, Bunkyo-ku, Tokyo 113-0033, Japan
[6]Centre for Space Research, Physics Department, North-West University, Potchefstroom 2520, South Africa
[7]Department of Physics and Astronomy, Faculty of Physical Sciences, University of Nigeria, Carver Building, 1 University Road, Nsukka, Nigeria
[8]Max-Planck-Institut für Radioastronomy, Auf dem Hügel 69, D-53121-Bonn, Germany
[9]Toyo University, 5-28-20 Hakusan, Bunkyo-ku, Tokyo 112-8606, Japan
[10]Graduate School of Science and Engineering, Kagoshima University, 1-21-35 Korimoto, Kagoshima, Kagoshima 890-0065, Japan
[11]Amanogawa Galaxy Astronomy Research Center, Graduate School of Science and Engineering, Kagoshima University, 1-21-35 Korimoto, Kagoshima, Kagoshima 890-0065, Japan

[12]Faculty of Science, Kagoshima University, 1-21-35 Korimoto, Kagoshima, Kagoshima 890-0065, Japan

[13]Center for General Education, Institute for Comprehensive Education, Kagoshima University, 1-21-30 Korimoto, Kagoshima, Kagoshima 890-0065, Japan

[14]Korea Astronomy and Space Science Institute, Hwaam-dong 61-1, Yuseong-gu, Daejeon, 305-348, Republic of Korea

[15]Teikyo University of Science, 2-2-1 Senju-Sakuragi, Adachi-ku, Tokyo 120-0045, Japan

[16]Graduate School of Sciences and Technology for Innovation, Yamaguchi University, 1677-1 Yoshida, Yamaguchi, Yamaguchi 753-8512, Japan

[17]NAOJ ALMA Project, National Astronomical Observatory of Japan, 2-21-1 Osawa, Mitaka, Tokyo 181-8588, Japan

[18]National Astronomical Research Institute of Thailand, 260 Moo 4, T. Donkaew, Amphur Maerim, Chiang Mai, 50180, Thailand

[19]National Time Service Center, Key Laboratory of Precise Positioning and Timing Technology, Chinese Academy of Sciences, Xi'an 710600, People's Republic of China

*E-mail: tomoya.hirota@nao.ac.jp

Abstract

We present the first astrometry catalog from the Japanese VLBI (very long baseline interferometer) project VERA (VLBI Exploration of Radio Astrometry). We have compiled all the astrometry results from VERA, providing accurate trigonometric-annual-parallax and proper-motion measurements. In total, 99 maser sources are listed in the VERA catalog. Among them, 21 maser sources are newly reported, while the rest of the 78 sources are referred to in previously published results or those in preparation for forthcoming papers. The accuracy in the VERA astrometry is revisited and compared with that from the other VLBI astrometry projects such as BeSSeL (The Bar and Spiral Structure Legacy) Survey and GOBELINS (the Gould's Belt Distances Survey) with the VLBA (Very Long Baseline Array). We have confirmed that most of the astrometry results are consistent with each other, and the largest error sources are due to source structure of the maser features and their rapid variation, along with the systematic calibration errors and different analysis methods. Combined with the BeSSeL results, we estimate the up-to-date fundamental Galactic parameters of $R_0 = 7.92 \pm 0.16_{\mathrm{stat.}} \pm 0.3_{\mathrm{sys.}}$ kpc and $\Omega_\odot = 30.17 \pm 0.27_{\mathrm{stat.}} \pm 0.3_{\mathrm{sys.}}$ km s^{-1} kpc^{-1}, where R_0 and $\Omega_\odot$ are the distance from the Sun to the Galactic center and the Sun's angular velocity of the Galactic circular rotation, respectively.

Key words: astrometry — Galaxy: fundamental parameters — masers

1 Introduction

The distance toward an astronomical object is the most fundamental parameter in astronomy and astrophysics. All the physical and dynamical properties of the target sources are estimated based on their distances. The most accurate and reliable method for distance determination is the trigonometric annual parallax measurements. For this reason, the Hipparcos (Kovalevsky 1998) and the very recent GAIA data release 2 (DR2) (Gaia Collaboration 2018) have presented optical astrometry databases for more than 10^5 and 10^9 parallaxes for visible stars with accuracies of 1 mas and a few $10\,\mu$as, respectively. The large number of optical astrometry data play important roles for understanding not only basic properties of each target source but also statistics of various kinds of stellar samples such as the Hertzsprung–Russell (HR) diagram, the period–luminosity relation of variable stars, and dynamics of the Milky Way Galaxy. However, it is not very easy to access distant sources in the Galactic disk through observations at optical bands because of the extremely high optical extinction. In particular, it is crucial to determine

the source distances toward dust/molecular clouds which are seen in the optical and sometimes infrared dark clouds.

To overcome the above issues, radio astrometry observations have been developed in the last two decades by utilizing the very long baseline interferometer (VLBI) technique (Reid & Honma 2014). When the VLBI array consists of 1000 km baselines, a synthesized beam size (full-width half-maximum, FWHM) of the order of 1 milli-arcsecond (mas) is achievable, as roughly evaluated by $\theta_{mas} \sim 2000 \times \lambda_{cm}/D_{km}$, where λ_{cm} and D_{km} are the observed wavelength in centimeters and the maximum baseline length in kilometers, respectively. Furthermore, high signal-to-noise ratios (SNR) allow us to measure more accurate positions of target sources than the beam size with the random (or thermal) error of $\sim \theta_{mas}/2SNR$ (Reid et al. 1988). Usually, the absolute position error in the VLBI astrometry is dominated by the systematic calibration error expressed as $\sim c\Delta\tau\theta_{SA}/D$, where c, $\Delta\tau$, and θ_{SA} are the speed of light, residual delay in calibration, and separation angle between the target source and calibrator (Reid & Honma 2014), respectively. If careful phase calibrations are successfully conducted, the high accuracy of VLBI astrometry yields the trigonometric parallax for the 10 kpc (corresponding to 0.1 mas parallax) sources in the Galaxy (Sanna et al. 2017; Nagayama et al. 2020b).

For this purpose, the VLBI Exploration of Radio Astrometry (VERA) project was initiated in early 2000 by the National Astronomical Observatory of Japan (NAOJ). VERA is designed for the purpose of the VLBI astrometry to reveal three-dimensional velocity and spatial structures in the Galaxy. The observational targets are mostly limited to strong maser sources distributed across the Galaxy, with nearby position (phase) calibrators. The construction was completed in 2002 followed by scientific verification observations to establish a method for accurate calibration and astrometry data analysis. Regular operations of VERA observations were started in 2004 and the first astrometry results were published in 2007 (Honma et al. 2007; Hirota et al. 2007). As of the end of 2019, more than 60 papers have been published to report results of VERA astrometry observations of Galactic maser sources associated with young stellar objects (YSOs) and late-type stars mostly in the asymptotic giant branch (AGB) and red supergiant (RSG) stars, as summarized in table 1.

At almost the same time, the Very Long Baseline Array (VLBA) legacy program named The Bar and Spiral Structure Legacy (BeSSeL) Survey has also been carrying out intensive VLBI astrometry observations mainly for distant Galactic high-mass star-forming regions (SFRs) associated with masers (Reid et al. 2009a). Other VLBI arrays, such as the European VLBI Network (EVN) and the Australian Long Baseline Array (LBA), are also conducting

VLBI astrometry for maser sources in high-mass SFRs by using 6.7 GHz CH_3OH masers (Rygl et al. 2010; Krishnan et al. 2015, 2017). As for low-mass nearby SFRs, another VLBA legacy survey, Gould's Belt Distances Survey (GOBELINS), observes non-thermal radio emission from T-Tauri stars to measure their trigonometric annual parallaxes (Loinard et al. 2008; Dzib et al. 2016; Kounkel et al. 2017; Ortiz-León et al. 2017, 2018a). Along with these surveys, a number of VLBI astrometry observations have been applied to various populations of stellar radio emissions (Reid & Honma 2014).

The primary aim of this paper is to compile all the published astrometry results from VERA to establish the first VERA catalog (section 4). We also report on some new astrometry results from VERA. The results are compared with those of the other VLBI astrometry projects, BeSSeL (subsection 5.1) and GOBELINS (subsection 5.2). Based on the latest VERA astrometry dataset, we revisit their accuracy and possible error sources of astrometry (subsection 5.3). Thus, we mainly concentrate on the maser astrometry data for the samples of YSOs in SFRs and AGBs/RSGs in the present paper. The up-to-date Galactic constants are estimated using all the available VLBI astrometry data (subsection 5.4) based on similar methods discussed previously (Reid et al. 2009b, 2014, 2019; Honma et al. 2012, 2015).

2 Observations

Although details are described in each paper, here we summarize general information about VERA astrometry observations. VERA is consisted of four 20 m radio telescopes in Japan; at Mizusawa, Iriki, Ogasawara, and Ishigaki-jima stations. The baseline lengths of VERA, ranging from 1020 to 2270 km, provide synthesized beam sizes of 1.2 mas at 22 GHz and 0.7 mas at 43 GHz. We have mainly carried out astrometry observations using the $6_{1,6}$–$5_{2,3}$ transition of H_2O at 22.235080 GHz (Pickett et al. 1998). Some of the observations have been conducted for the $J = 1$–0 SiO maser transitions at 43.122075 GHz and 42.820586 GHz for $v = 1$ or/and $v = 2$, respectively (Müller et al. 2001). To measure trigonometric annual parallaxes of maser sources, we usually carry out monitoring observations for at least one year and sometimes two years or longer. In some cases, monitoring observations are interrupted due to the shorter life time of the target masers. A typical interval of monitoring is one–two months depending on the variability of masers; more variable sources such as AGB stars and low-mass YSOs are observed in shorter interval than one month. To achieve better UV coverage, each epoch of observation lasts from horizon to horizon for about 5–10 hours depending on the source declination (i.e.,

Table 1. Astrometry results from VERA.*

Name	RA (J2000.0) (h m s)	Dec (J2000.0) (° ' ")	l (°)	b (°)	π_{VERA} (mas)	σ_{VERA} (mas)	μ_x (mas yr⁻¹)	$\Delta\mu_x$ (mas yr⁻¹)	μ_y (mas yr⁻¹)	$\Delta\mu_y$ (mas yr⁻¹)	v_{lsr} (km s⁻¹)	Δv_{lsr} (km s⁻¹)	Type	References
SY Scl	00 07 36.2476	−25 29 40.028	039.91	−80.04	0.75	0.03	+5.57	0.04	−7.32	0.12	+22.0	5.0	AGB	Nyu et al. (2011)
IRAS 00259+5625	00 28 43.5075	+56 41 56.868	119.80	−06.03	0.412	0.123	−2.48	0.32	−2.85	0.65	−38.3	3.1	SFR	Sakai et al. (2014)
NGC 281	00 52 24.7008	+56 33 50.527	123.06	−06.30	0.355	0.030	−2.63	0.05	−1.86	0.08	−30.0	5.0	SFR	Sato et al. (2008)
G125.51+02.03	01 15 40.8027	+64 46 40.766	125.51	+02.03	0.145	0.023	−1.20	0.21	−0.33	0.27	−57.0	9.0	SFR	Koide et al. (2019), Sakai et al. (2020)†
W 3(H₂O)	02 27 04.6800	+61 52 24.566	133.94	+01.06	0.527	0.016	+0.27	0.29	−1.24	0.15	−55.6	1.2	SFR	Matsumoto et al. (2011), Nagayama et al. (2020a)†
G135.28+02.80	02 43 28.5825	+62 57 08.390	135.28	+02.80	0.124	0.011	−0.45	0.20	+0.09	0.16	−72.9	1.6	SFR	Nagayama et al. (2020b)
G137.07+03.00	02 58 13.1793	+62 20 32.915	137.07	+03.00	0.187	0.016	−0.57	0.16	−0.01	0.16	−50.1	0.4	SFR	Nagayama et al. (2020b)
L 1448 C	03 25 38.8784	+30 44 05.252	157.57	−21.94	4.31	0.33	+21.90	0.70	−23.10	3.30	+5.0	5.0	SFR	Hirota et al. (2011)
NGC 1333 SVS13	03 29 03.7247	+31 16 03.802	158.35	−20.56	4.25	0.32	+14.25	2.58	−9.95	0.74	+8.0	5.0	SFR	Hirota et al. (2008a)
V637 Per	03 54 02.2577	+36 32 17.926	159.10	−13.20	0.94	0.02	−0.61	0.43	−0.90	0.37	−97.8	0.9	AGB	Present paper
L 1482	04 30 27.4008	+35 09 17.649	165.47	−09.05	1.879	0.096	+3.07	0.06	−8.60	0.04	+1.0	5.0	SFR	Omodaka et al. (2020)
BX Eri	04 40 32.7762	−14 12 02.710	211.48	−35.33	2.116	0.105	+6.77	0.35	−10.79	0.25	−0.3	0.1	AGB	Present paper
T Lep	05 04 50.8430	−21 54 16.505	222.67	−32.71	3.06	0.04	+14.60	0.50	−35.43	0.79	−27.6	5.0	AGB	Nakagawa et al. (2014)
IRAS 05137+3919	05 17 13.7410	+39 22 19.880	168.06	+00.82	0.086	0.027	+0.30	0.27	−0.89	0.73	−27.0	5.0	SFR	Honma et al. (2011)
BW Cam	05 19 52.1643	+63 15 54.684	143.43	+20.09	0.749	0.189	+7.55	1.19	−19.63	0.81	+42.0	0.7	AGB	Present paper
IRAS 05168+3634	05 20 22.0700	+36 37 56.630	170.66	−00.25	0.532	0.053	+0.23	1.07	−3.14	0.28	−15.5	1.9	SFR	Sakai et al. (2012)
AFGL 5142	05 30 48.0173	+33 47 54.568	174.20	−00.07	0.467	0.010	+0.32	0.27	−0.22	0.47	−2.0	5.0	SFR	Burns et al. (2017)
Orion KL	05 35 14.5050	−05 22 30.450	209.00	−19.38	2.39	0.03	+9.56	0.10	−3.83	0.15	+3.0	5.0	SFR	Hirota et al. (2007), Kim et al. (2008),† Nagayama et al. (2020a)
WB 673	05 38 00.3500	+35 58 58.400	173.17	+02.36	0.590	0.043	+0.01	0.03	−3.40	0.09	−10.4	0.2	SFR	Present paper
RW Lep	05 38 52.7260	−14 02 27.180	217.78	−22.30	1.62	0.16	+15.80	2.10	−31.20	2.10	−59.0	1.0	AGB	Kamezaki et al. (2014b)
L 1641 S3	05 39 56.0431	−07 30 27.988	211.57	−19.29	2.114	0.127	−11.68	0.67	−7.74	0.36	+6.8	4.2	SFR	Present paper
S 235AB MIR	05 40 53.3800	+35 41 48.500	173.72	+02.70	0.639	0.033	+0.08	0.12	−2.41	0.14	−17.0	5.0	SFR	Burns et al. (2015)
B 35	05 44 29.2483	+09 08 52.121	196.93	−10.40	1.98	0.25	−2.30	0.53	−5.31	0.59	+12.0	1.0	SFR	Present paper
BX Cam	05 46 44.3251	+69 58 24.408	143.43	+20.09	1.73	0.03	+13.48	0.14	−34.30	0.18	0.0	5.0	AGB	Matsuno et al. (2020)
G192.16−03.81	05 58 13.5300	+16 31 58.900	192.16	−03.81	0.66	0.04	+0.69	0.15	−1.57	0.15	+5.7	5.0	SFR	Shiozaki et al. (2011)
IRAS 06058+2138	06 08 53.4938	+21 38 30.741	188.94	+00.88	0.569	0.034	+1.06	0.18	−2.77	0.34	+3.0	5.0	SFR	Oh et al. (2010)
IRAS 06061+2151	06 09 06.9746	+21 50 41.405	188.79	+01.03	0.496	0.031	−0.10	0.10	−3.91	0.07	−1.6	0.2	SFR	Niinuma et al. (2011)
HH 12-15	06 10 50.1400	−06 11 45.600	213.88	−11.84	1.61	0.36	−0.36	1.68	+3.17	0.47	+11.3	2.0	SFR	Present paper
S 255 IR-SMA1	06 12 54.0064	+17 59 22.959	192.60	−00.05	0.563	0.036	−0.13	0.20	−0.06	0.27	+5.3	5.0	SFR	Burns et al. (2016)
S 269	06 14 37.0800	+13 49 36.700	196.45	−01.67	0.189	0.008	−0.42	0.20	−0.12	0.20	+18.0	5.0	SFR	Honma et al. (2007),† Asaki et al. (2014)

Table 1. (Continued)

Name	RA (J2000.0) (h m s)	Dec (J2000.0) (° ′ ″)	l (°)	b (°)	$\pi_{\rm VERA}$ (mas)	$\sigma_{\rm VERA}$ (mas)	μ_x (mas yr⁻¹)	$\Delta\mu_x$	μ_y (mas yr⁻¹)	$\Delta\mu_y$	$v_{\rm lsr}$ (km s⁻¹)	$\Delta v_{\rm lsr}$	Type	References
G200.08−01.63	06 21 47.5742	+10 39 22.811	200.08	−01.63	0.200	0.017	+0.32	0.14	−0.14	0.16	+36.3	0.6	SFR	Nagayama et al. (2020b)
U Lyn	06 40 46.4853	+59 52 01.490	155.66	+21.94	1.27	0.06	+0.80	0.57	−6.00	0.56	−13.0	3.0	AGB	Kamezaki et al. (2016a)
NGC 2264	06 41 09.8600	+09 29 14.700	203.32	+02.05	1.356	0.098	−1.08	0.58	−5.92	3.06	+7.0	3.0	SFR	Kamezaki et al. (2014a)
WB 886	06 47 13.3000	+00 26 05.920	212.06	−00.74	0.349	0.052	−0.40	0.94	+0.37	0.33	+45.0	3.0	SFR	H. Nakanishi et al. (in preparation)
NSV 17351	07 07 49.3869	−10 44 05.998	224.34	−01.29	0.247	0.010	−1.19	0.11	+1.30	0.19	−50.1	1.9	AGB	A. Morita et al. (in preparation)
VY CMa	07 22 58.3291	−25 46 03.141	239.35	−05.06	0.88	0.08	−2.09	0.16	+1.02	0.61	+20.0	5.0	RSG	Choi et al. (2008)
OZ Gem	07 33 57.7500	+30 30 37.799	188.80	+21.90	0.806	0.039	−1.97	0.32	−8.69	0.21	+8.7	1.4	AGB	Urago et al. (2020)
QX Pup	07 42 16.9470	−14 42 50.200	231.84	+04.22	0.61	0.03	−4.76	0.37	−0.94	0.62	+33.0	5.0	AGB	M. Ooyama et al. (in preparation)
IRAS 07427−2400	07 44 51.9200	−24 07 41.500	240.31	+00.07	0.185	0.027	−1.79	0.32	+2.60	0.17	+66.4	5.0	SFR	Sakai et al. (2015)
HU Pup	07 55 40.1843	−28 38 54.608	245.44	−00.15	0.308	0.042	−1.16	0.15	+3.69	0.20	+43.9	0.6	AGB	Present paper
R Cnc	08 16 33.8243	+11 43 34.518	211.75	+24.14	3.84	0.29	+1.24	0.34	−11.57	0.97	+16.9	5.0	AGB	Present paper
X Hya	09 35 30.2650	−14 41 28.639	248.15	+26.70	2.07	0.05	−51.37	0.97	−15.02	1.47	+27.3	5.0	AGB	Present paper
R UMa	10 44 38.4283	+68 46 32.344	138.36	+44.36	1.97	0.05	−40.77	0.39	−24.75	0.38	+40.5	1.0	AGB	Nakagawa et al. (2016)
W Leo	10 53 37.4325	+13 42 54.367	233.02	+59.43	1.03	0.02	−6.84	0.09	−8.65	0.08	+46.7	0.2	AGB	Present paper
HS UMa	11 35 30.6878	+34 52 04.006	182.78	+72.02	2.816	0.095	−11.48	0.17	−10.86	0.65	+1.6	0.3	AGB	Present paper
S Crt	11 52 45.9697	−07 35 48.096	278.59	+52.48	2.33	0.13	−3.17	0.22	−5.41	0.22	+37.9	5.0	AGB	Nakagawa et al. (2008)
R Hya	13 29 42.7819	−23 16 52.775	314.22	+38.75	7.93	0.18	−53.79	1.05	+16.15	1.83	−8.5	5.0	AGB	Present paper
RX Boo	14 24 11.6206	+25 42 12.909	034.28	+69.21	7.31	0.50	+24.55	1.06	−49.67	2.38	+1.0	5.0	AGB	Kamezaki et al. (2012)
FV Boo	15 08 25.7530	+09 36 18.390	011.03	+53.27	0.97	0.06	+6.81	0.14	+1.01	0.12	+7.5	1.0	AGB	Kamezaki et al. (2016b)
Y Lib	15 11 41.2990	−06 00 41.462	353.83	+42.59	0.855	0.050	−10.15	2.39	−15.02	4.26	+14.4	1.1	AGB	Chibueze et al. (2019)
S Ser	15 21 39.5334	+14 18 53.107	020.50	+52.79	1.25	0.04	−2.56	1.42	+5.20	2.31	+25.1	5.0	AGB	Present paper
IRAS 16293−2422	16 32 22.8500	−24 28 36.400	353.94	−15.84	5.6	1.5	−20.60	0.70	−32.40	2.00	+3.0	5.0	SFR	Imai et al. (2007)
NGC 6334I(N)	17 20 55.1920	−35 45 03.770	351.44	+00.65	0.789	0.161	−2.88	0.30	+3.23	0.39	−2.8	0.5	SFR	Chibueze et al. (2014a)
G353.27+00.64	17 26 01.5883	−34 15 14.903	353.27	+00.64	0.59	0.06	+0.47	0.07	+0.99	1.04	−5.0	5.0	SFR	Motogi et al. (2016)
G359.62−00.25	17 45 39.0908	−29 20 26.294	359.62	−00.25	0.33	0.14	+1.31	0.33	−2.41	0.87	−80.0	5.0	SFR	Iwata et al. (2017)
Sgr B2	17 47 20.1817	−28 23 03.889	000.67	−00.03	0.133	0.038	−1.83	0.21	−3.70	0.09	+62.0	5.0	SFR	D. Sakai et al. (in preparation)
Sgr D	17 48 48.5450	−28 01 26.290	001.15	−00.12	0.423	0.083	−0.76	0.15	−2.88	0.34	−18.0	5.0	SFR	Sakai et al. (2017)
G005.88−00.39	18 00 30.3100	−24 04 04.500	005.88	−00.39	0.78	0.05	−0.17	0.60	−0.95	0.48	+9.0	3.0	SFR	Motogi et al. (2011)
G007.47+00.06	18 02 13.1790	−22 27 58.960	007.47	+00.06	—	—	−2.42	0.09	−4.39	0.08	−15.0	5.0	SFR	Yamauchi et al. (2016)‡
G014.33−00.64	18 18 54.6532	−16 47 50.077	014.33	−00.64	0.893	0.101	+0.95	2.00	−2.50	2.00	+22.0	5.0	SFR	Sato et al. (2010)
M 17	18 20 23.0160	−16 11 48.030	015.03	−00.67	0.491	0.041	−0.51	0.21	−2.04	0.21	+20.0	5.0	SFR	Chibueze et al. (2016)
G021.88+00.02	18 31 01.7490	−09 49 01.130	021.88	+00.01	—	—	−3.30	0.06	−5.33	0.22	+26.9	0.4	SFR	Present paper‡
IRAS 18286−0959	18 31 22.9340	−09 57 21.700	021.80	−00.13	0.277	0.041	−3.20	0.30	−7.20	0.20	+60.0	5.0	AGB	Imai et al. (2013)
G034.39+00.22	18 53 18.7700	+01 24 08.800	034.39	+00.22	0.643	0.049	−0.25	0.80	—	—	+58.0	5.0	SFR	Kurayama et al. (2011)‡
S 76 E	18 56 11.4413	+07 53 17.608	040.50	+02.54	0.521	0.024	−0.89	0.34	−2.27	0.56	+31.9	1.7	SFR	Chibueze et al. (2017)
G037.50+00.53	18 57 53.3876	+04 18 17.394	037.50	+00.53	0.091	0.016	−2.74	0.18	−5.49	0.10	+10.7	2.6	SFR	Nagayama et al. (2020b)
G037.82+00.41	18 58 53.8800	+04 32 15.004	037.82	+00.41	0.089	0.020	−2.73	0.12	−5.53	0.12	+17.5	0.8	SFR	Nagayama et al. (2020b)
W 48 A	19 01 45.5423	+01 13 32.573	035.20	−01.74	0.433	0.026	−0.05	0.81	−3.51	0.38	+41.9	1.4	SFR	Chibueze et al. (2020)

Table 1. (Continued)

Name	RA (J2000.0) (h m s)	Dec (J2000.0) (° ′ ″)	l (°)	b (°)	$\pi_{\rm VERA}$ (mas)	$\sigma_{\rm VERA}$ (mas)	μ_x (mas yr⁻¹)	$\Delta\mu_x$ (mas yr⁻¹)	μ_y (mas yr⁻¹)	$\Delta\mu_y$ (mas yr⁻¹)	$v_{\rm lsr}$ (km s⁻¹)	$\Delta v_{\rm lsr}$ (km s⁻¹)	Type	References
G044.31+00.04	19 12 15.7930	+10 07 53.085	044.31	+00.04	0.192	0.031	−3.36	0.05	−6.92	0.06	+57.8	0.5	SFR	Present paper
G048.60+00.02	19 20 31.1772	+13 55 25.257	048.60	+00.02	0.199	0.007	−2.76	0.04	−5.28	0.11	+19.0	1.0	SFR	Nagayama et al. (2011a)
G048.99−00.30	19 22 26.1348	+14 06 39.133	048.99	−00.30	0.178	0.017	−2.16	0.09	−5.87	0.17	+66.3	0.3	SFR	Nagayama et al. (2015a)
G049.19−00.33	19 22 57.7705	+14 16 09.969	049.19	−00.33	0.211	0.016	−3.21	0.07	−5.08	0.25	+69.9	0.5	SFR	Nagayama et al. (2015a)
IRAS 19213+1723	19 23 37.3229	+17 29 10.479	052.10	+01.04	0.251	0.036	−2.53	0.04	−6.07	0.05	+41.7	5.0	SFR	Oh et al. (2010)
K 3-35	19 27 44.0230	+21 30 03.440	056.10	+02.09	0.260	0.040	−3.34	0.10	−5.93	0.07	+26.0	5.0	AGB	Tafoya et al. (2011)
IRAS 19312+1950	19 33 24.2430	+19 56 55.650	055.37	+00.19	0.263	0.047	−2.61	0.47	−6.73	0.14	+36.0	1.0	SFR	Imai et al. (2011)
G061.48+00.10	19 46 47.9175	+25 12 52.698	061.48	+00.10	0.454	0.022	−1.31	0.16	−6.39	0.34	+41.7	6.2	SFR	Present paper
SY Aql	20 07 05.4083	+12 57 06.219	053.37	−10.31	1.10	0.07	+12.26	0.11	−15.93	0.22	−44.8	5.0	AGB	Present paper
IRAS 20056+3350	20 07 31.2586	+33 59 41.477	071.31	+00.83	0.213	0.026	−2.62	0.33	−5.65	0.52	+9.4	5.0	SFR	Burns et al. (2014b)
ON 1	20 10 09.2045	+31 31 36.101	069.54	−00.97	0.404	0.017	−3.10	0.18	−4.70	0.24	+12.0	1.0	SFR	Nagayama et al. (2011b)
IRAS 20126+4104	20 14 26.0218	+41 13 32.674	078.12	+03.63	0.750	0.092	−4.15	0.51	−4.07	0.51	−3.5	4.0	SFR	Nagayama et al. (2015b)
IRAS 20143+3634	20 16 13.3617	+36 43 33.920	074.57	+00.85	0.367	0.037	−2.99	0.16	−4.37	0.43	−1.0	1.0	SFR	Burns et al. (2014a)
ON 2 N	20 21 44.0123	+37 26 37.484	075.78	+00.34	0.261	0.009	−2.79	0.13	−4.66	0.17	+0.0	1.0	SFR	Ando et al. (2011)
IRAS 20231+3430	20 25 07.8013	+34 50 34.733	074.04	−01.71	0.611	0.022	−3.79	0.18	−4.88	0.25	+6.0	5.0	SFR	Ogbodo et al. (2017)
IRAS 20255+4032	20 27 20.2734	+40 42 34.648	079.09	+01.33	0.118	0.035	−2.49	0.13	−3.36	0.23	−18.2	5.0	SFR	N. Sakai et al. (in preparation)
G080.70+00.70	20 35 09.1650	+41 38 20.260	080.70	+00.70	0.258	0.022	−3.18	0.09	−5.09	0.07	−2.3	0.7	SFR	Present paper
G095.05+03.97	21 15 55.6798	+54 43 31.328	095.05	+03.97	0.108	0.023	−2.44	0.21	−2.63	0.17	−87.0	5.0	SFR	Sakai et al. (2020),† H. Nakanishi et al. (in preparation)
G097.53+03.18	21 32 12.4400	+55 53 49.600	097.53	+03.18	0.177	0.028	−2.64	0.20	−2.38	0.22	−73.0	5.0	SFR	Sakai et al. (2020),* H. Nakanishi et al. (in preparation)
IRAS 21379+5106	21 39 40.5500	+51 20 34.000	095.29	−00.93	0.262	0.031	−2.74	0.08	−2.87	0.18	−42.3	0.2	SFR	Nakanishi et al. (2015)
AFGL 2789	21 39 58.2717	+50 14 21.014	094.60	−01.79	0.326	0.031	−2.20	0.08	−3.77	0.15	−44.0	5.0	SFR	Oh et al. (2010)
G102.35+03.64	21 57 25.1841	+59 21 56.614	102.35	+03.64	0.154	0.021	−2.53	0.33	−2.14	0.33	−88.0	5.0	SFR	Sakai et al. (2020),* H. Nakanishi et al. (in preparation)
SV Peg	22 05 42.0850	+35 20 54.536	088.72	−16.29	3.00	0.06	+11.59	0.54	−8.63	0.44	+3.9	5.0	AGB	Sudou et al. (2019)
S 140	22 19 17.4657	+63 18 39.851	106.79	+05.31	1.154	0.069	−6.16	0.12	−4.74	0.11	−6.1	5.0	SFR	Present paper
IRAS 22198+6336	22 21 26.7279	+63 51 37.924	107.29	+05.63	1.309	0.047	−2.47	1.40	+0.26	1.40	−11.0	5.0	SFR	Hirota et al. (2008b)
IRAS 22480+6002	22 49 58.8760	+60 17 56.650	108.43	−00.89	0.400	0.025	−2.58	0.33	−1.91	0.17	−50.8	3.5	SFR	Imai et al. (2012)
IRAS 22555+6213	22 57 29.8090	+62 29 46.850	110.20	+02.48	0.314	0.070	−2.04	0.05	−0.66	0.06	−63.0	1.0	SFR	Chibueze et al. (2014b)
IRAS 23004+5642	23 02 32.0800	+56 57 51.400	108.47	−02.81	0.309	0.010	−2.45	1.00	−3.00	0.70	−54.0	5.0	SFR	H. Nakanishi et al. (in preparation)
R Peg	23 06 39.1652	+10 32 36.078	085.41	−44.56	2.76	0.28	+3.60	1.53	−6.44	0.92	+22.5	5.0	AGB	Present paper
R Aqr	23 43 49.4616	−15 17 04.202	066.52	−70.33	4.59	0.24	+37.13	0.47	−28.62	0.44	−21.5	5.0	AGB	Kamohara et al. (2010), Min et al. (2014)*
PZ Cas	23 44 03.2816	+61 47 22.187	115.06	−00.05	0.356	0.026	−3.70	0.20	−2.00	0.30	−36.2	0.7	RSG	Kusuno et al. (2013)

*The ASCII format file of this table is available in the supplementary data section of the online edition.

†If there are multiple references, the data with smaller parallax errors noted with * is employed.

‡Their parallax and/or proper motions cannot be determined.

maximum elevation). In a single horizon–horizon track, we observe one or two maser sources. In case of observations of two different sources, we switch the target sources every 10 minutes.

VERA astrometry observations are carried out with the dual-beam receiving system (Honma et al. 2008a). A pair of target maser source and reference continuum source (calibrator) are observed with two receivers simultaneously. The separation angle of these two sources is limited to 0°.3–2°.2. Reference sources are mainly selected from the VLBA Calibrator Catalog (Beasley et al. 2002), for which the absolute positions are determined with ∼ sub-mas accuracy. Some of the calibrators have been newly detected by using fringe-check survey observations with VERA at 22 GHz and/or 43 GHz (Petrov et al. 2007, 2012). In addition to reference sources, bandpass and delay calibrator(s) are observed every 60–80 min. Amplitude calibrations are done through the chopper-wheel method (Ulich & Haas 1976). Typical system noise temperatures are 100 K at 22 GHz and 200 K at 43 GHz, under good weather conditions. However, they become higher by a factor of 2 or larger (>200 K at 22 GHz and >400 K at 43 GHz) under the conditions of high humidity and temperature, in particular at the southern isolated islands, Ogasawara and Ishigaki stations, and/or in the summer season.

VERA can configure various frequency settings and recording settings, such as spectral resolution, total bandwidths, number of intermediate frequency (IF) channels, and spectral channels within each IF. Details of the setup in each observation can be seen in the respective original papers. In most of observations, the digital filter output provides 16 IF channels with 16 MHz bandwidth (Iguchi et al. 2005). Only left-handed circular polarization is received and sampled with 2 bits per second at 1 Gbps. Dual-polarization observation mode is under development at this moment. One of the 16 MHz IF channels is assigned to the target maser source and the rest of the 15 IF channels are assigned to the reference source. For masers, a spectral resolution is set to be 15.625 kHz or 31.25 kHz, corresponding to a velocity resolution of 0.21–0.42 km s^{-1} at 22 GHz or 0.11–0.22 km s^{-1} at 43 GHz. Data were recorded with magnetic tapes before 2015, while more recently hard disk recording system has been employed. The newly developed system is capable of wider-band recoding up to 16 Gbps (Oyama et al. 2016). Correlation processing was carried out with the FX hardware correlator located at the NAOJ Mitaka campus until early in 2015 (Chikada et al. 1991). From 2015, the regular operation of newly developed software correlator has been taking place in NAOJ Mizusawa campus (Oyama et al. 2016). The accumulation period in the correlation process is 1 second to produce visibility data for further post-processing data analysis.

To achieve accurate phase calibration, reference sources are required to have flux densities higher than ∼ 50–100 mJy on average (in the case of the 1 Gbps recording rate) to detect their fringes with an *SNR* of at least 5 within a coherence time of 1–2 min and the recording bandwidths of 240 MHz under the best weather conditions. Target maser sources are detectable with the peak intensities of ∼ 1 Jy beam^{-1} after successful phase-referencing analysis.

3 Data analysis

Basic procedures for calibration and synthesis imaging are summarized in the early results from VERA (Honma et al. 2007; Hirota et al. 2007). Calibration processes and their accuracies, in particular possible error sources by atmospheric calibration, station positions, dual-beam calibration, and source structure effects, are reported in separate papers (Honma et al. 2008a, 2008b, 2010; Nagayama et al. 2020b). Only the overall characteristics of astrometric accuracy are discussed in the present paper.

Before the calibration, delay tracking models are recalculated using a software based on the CALC software package developed for the geodetic VLBI observations (Manabe et al. 1991; Jike et al. 2009) because a priori models employed in the correlation processing are inaccurate for astrometry. In the recalculations, phase-tracking center positions of the target maser sources are shifted to the actual position of maser features within ∼ 100 mas. In the subsequent astrometry calibrations, more accurate delay tracking is done using the following datasets: Tropospheric and ionospheric delays are recalculated based on the GPS measurements and meteorological data (Honma et al. 2008b; Nagayama et al. 2020b), the earth orientation parameters are taken from the International Earth rotation and Reference systems Service (IERS), and the antenna positions are measured through regular monthly geodetic observations with VERA at 22 GHz (Jike et al. 2009, 2018). For the dual-beam observations, path lengths between two receiving systems for masers and reference sources are calibrated by injecting an artificial noise source on the dishes (Honma et al. 2008a), which is the so-called "horn-on-dish method." Overall calibration errors are estimated to be 10–20 mm for the tropospheric zenith delay, 3–10 Total Electron Content Unit (TECU) for the ionospheric delay, 3 mm for the antenna position, and 0.1 mm for the instrumental optical path lengths between two beams, as summarized in Nagayama et al. (2020b) and references therein.

Other calibration processes are done in a standard manner of VLBI observations using the NRAO Astronomical Image Processing System (AIPS) software package.

Amplitude calibrations are done using the AIPS tasks APCAL and ACCOR, while a template method is employed using the AIPS task ACFIT in the case of problems in the chopper-wheel methods. The instrumental delays and phase offsets among all of the IF channels are determined by the AIPS task FRING on strong calibrator sources, and residual phases are also determined by the AIPS task FRING on reference sources. These delay and phase calibration solutions are copied to the target maser sources by the AIPS task TACOP, and are applied to the target maser sources by the AIPS tack CLCAL. If the reference sources are too weak to detect fringes, so-called inverse phase-referencing is carried out in which maser sources are used for phase calibration (Hirota et al. 2011; Imai et al. 2012; Burns et al. 2015). Synthesis imaging and deconvolution were performed using the AIPS task IMAGR.

After making images of target maser sources at all spectral channels in all observing epochs, each maser spot and its feature are identified. A maser spot is defined as an emission component of a single velocity channel and a feature is used for a group of spots in consecutive velocity channels at position coincident with each others. The maser spots and features are identified by Gaussian fitting (AIPS tasks JMFIT or SAD) with a certain threshold of noise levels in a single-channel map and integrated intensity images, respectively.

Some of the data are analyzed using the VEDA (VEra Data Analyzer) package developed by the VERA project for its own astrometry data (Honma et al. 2007, 2011; Niinuma et al. 2011; Chibueze et al. 2014a; Yamauchi et al. 2016). More details of the VEDA package will be presented in the forthcoming paper (Nagayama et al. 2020a).

The identified maser spots or features are used to determine their proper motions and trigonometric annual parallaxes by fitting the positional offsets in right ascension and declination as a function of time. The fitting parameters are the trigonometric annual parallax π, right ascension and declination offset with respect to the tracking center position at the first epoch of observation ($\Delta\alpha\cos\delta$, $\Delta\delta$), and proper motions in right ascension and declination (μ_x, μ_y) $\equiv$ ($\mu_\alpha\cos\delta$, μ_δ). If the astrometric accuracy is significantly worse in declination compared with that in right ascension due to different path length error in the atmospheric calibration (Nagayama et al. 2020b), only the latter data are employed to determine the parallax. If there are multiple maser spots or features, position offsets and proper motions for all the spots/features are fitted simultaneously with the common parallax value.

Usually, the post-fit residual of the fitting is much larger than the astrometric accuracy expected from the thermal noise. This can be interpreted that there could be systematic calibration errors in the fitting results. Thus, the errors of these best-fitting parameters are estimated by adding the noise floor to all the astrometry results in order to set the reduced χ^2 value of unity (Honma et al. 2007; Reid et al. 2009a). This additional noise floor is regarded as the total error of astrometry including both systematic and random (thermal) errors.

In the case of VERA, error estimation is different from paper to paper. If there are multiple masers, two different approaches have been employed: one is to derive proper motions for individual features and common parallax for all features simultaneously by the least squares fitting. In this case, the fitting error is regarded as the parallax uncertainty. The other method is to derive a parallax value for each maser feature and average all these values. In this case, the standard deviation of these parallaxes is regarded as an uncertainty. However, if the error source of astrometry is dominated by the calibration error of atmospheric phase fluctuation, they are common for all the features, and hence the averaged parallax (the latter case) would include systematic errors which are common for all parallax values. Thus, the formal uncertainty could underestimate the error in the averaged parallax value. Although astrometry analysis methods are different from source to source in table 1, future updates of the VERA catalogue will be done using the unified methods through the new data analysis software package VEDA (Nagayama et al. 2020a).

4 Results

In table 1, we compile all the parallax measurements that have been conducted with VERA to date. In total, 99 maser sources are listed. We include some sources in table 1 for which only parallax values are reported (i.e., no proper motion data). New astrometry results from VERA are reported for the first time for 21 sources in the present paper, while the others have been or will be published (last column of table 1). Most of the target sources are observed with the 22 GHz H_2O masers, and two sources, Orion KL (Kim et al. 2008) and R Aqr (Kamohara et al. 2010; Min et al. 2014), are observed in the 43 GHz vibrationally excited SiO masers. The numbers of YSOs in SFRs and late-type stars (AGBs and RSGs) are 68 and 31, respectively. Some of the target sources classified as AGBs include possible candidates of post-AGB stars or young planetary nebulae, such as IRAS 18286−0959 (Imai et al. 2013) and K3-35 (Tafoya et al. 2011). Since the populations of RSGs are relatively small, only two sources, VY CMa (Choi et al. 2008) and PZ Cas (Kusuno et al. 2013), are reported.

We refer to the astrometry data from the original papers as listed in the last column in table 1. The numbers of significant digits of astrometric parameters are different from source to source, depending on the relative uncertainties.

We simply set a uniform number of significant digits for the parameters in table 1 except for the parallax values, for which we follow the definition of the original papers.

For proper motions, some cases need additional consideration. When the target sources are associated with multiple maser features, much of the literature calculated their averages to estimate systemic motions which are regarded as representing those of central stars. On the other hand, if there are an insufficient number of maser feature(s) in a target source, a proper motion of single feature is used to estimate its systematic motion. If there is no explicit discussion on proper motions in the original paper, we calculate these values as mentioned above. In most of the VERA results, errors in the proper motions are determined by the formal uncertainties in the fitting in the case of sources with a single feature or the mean proper motions of multiple maser features. To ensure the use of an accurate estimate of the source systemic proper motion in modeling the Galactic rotation, it is necessary to separate observed proper motions into their respective contributions from the internal proper motions caused by jets, outflows, etc., and the true motion of the SFRs in the sky plane. In cases where the proper motions are symmetric or random, this can be done by simply averaging all measured proper motions. However, in asymmetrically sampled cases, or cases of few detected maser features, the average motion may misrepresent the source proper motion. This consequently introduces errors into the evaluation of the model parameters during the fitting. We did not consider such potential systematic uncertainties in the proper motions in table 1. However, if a large enough sample of sources is used then these errors introduced should be average out.

The radial velocities of the target sources, which are usually measured by the radio molecular lines such as CO and NH_3 or by the maser lines themselves, are also listed in table 1. Similarly, these radial velocities could result in a significant amount of uncertainties in the estimated three-dimensional velocity field of the Galaxy. In particular, the definition of the radial velocities would affect the estimation of the systemic velocity of the target sources depending on either average or central velocities of the maser features. It is known that the H_2O masers sometimes show extremely high velocity features, up to 10–$100\,km\,s^{-1}$, with respect to the systemic velocity (Motogi et al. 2016). For instance, one of the target sources, IRAS 20255+4032, shows an average velocity of the four maser features of $-63.3\,km\,s^{-1}$, while the systemic velocity is determined by the CO line to be $-18.2\,km\,s^{-1}$ (N. Sakai et al. in preparation). In such cases, maser data lead erroneous assumption of the systemic velocities. If there is no estimation of uncertainties in the radial velocity, we take into account these uncertainties of $5\,km\,s^{-1}$ as indicated in table 1. Although the
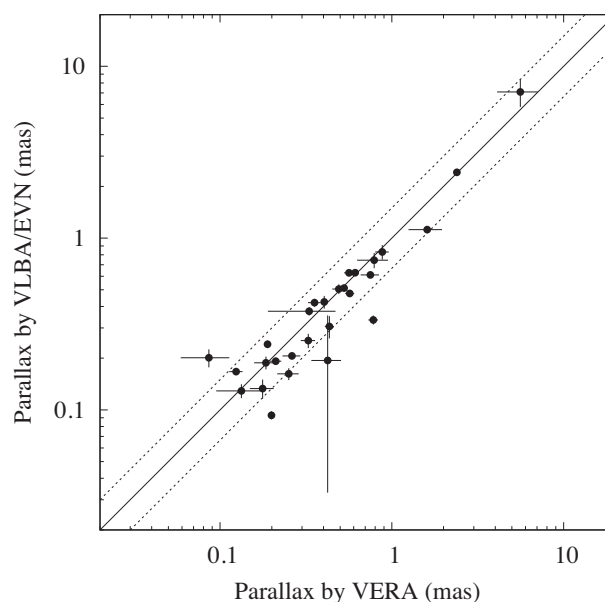

Fig. 1. Comparison of parallaxes from VERA and VLBA/EVN. A solid line indicates the VERA parallaxes equal to those of VLBA/EVN while dashed lines show their differences by factors of $1/1.5$ and 1.5.

BeSSeL project employs the more conservative value of $10\,km\,s^{-1}$, our results are not severely affected by these different assumptions.

5 Discussion

In this section, we revisit discussion on accuracy of the VERA astrometry and estimation of the Galactic fundamental parameters, as reported in previous summary papers (Reid et al. 2009b, 2014, 2019; Honma et al. 2012, 2015; Reid & Honma 2014).

5.1 Comparison with VERA and VLBA/EVN results

Figure 1 compares the results of parallax measurements carried out by VERA and VLBA/EVN. For this plot, most of the target sources are the H_2O and/or CH_3OH maser sources which are identified in the same SFRs within $1'$ as listed in table 2. Some of high-mass SFRs host multiple YSOs associated with different maser clusters within individual regions. We do not include such sources because they could be located in different molecular clouds aligned along the line-of-sight by chance. The only exceptions are Orion KL and HH 12-15 which are observed in radio continuum emission (Menten et al. 2007; Dzib et al. 2016). For Orion KL, we refer to Menten et al. (2007), although there are multiple/different VLBI astrometry results for different YSOs in the same region (see more discussion in the next subsection). To compare these VLBI astrometry

Table 2. Parallaxes from VERA and VLBA/EVN and their differences.

Name	π_{VERA} (mas)	$\pi_{\mathrm{VLBA/EVN}}$ (mas)	$\pi_{\mathrm{VERA}} - \pi_{\mathrm{VLBA/EVN}}$ (mas)	$\Delta\pi/\sigma_{\Delta\pi}$	References for VLBA/EVN*
NGC 281/NGC 281-W	0.355 ± 0.030	0.421 ± 0.022	-0.07 ± 0.04	-1.77	Rygl et al. (2010)
W 3(H_2O)/W 3(OH)	0.527 ± 0.016	0.512 ± 0.010	0.02 ± 0.02	0.79	Xu et al. (2006),[†] Hachisuka et al. (2006)
G135.28+02.80	0.124 ± 0.011	0.167 ± 0.006	-0.04 ± 0.01	-3.43	Hachisuka et al. (2009)
IRAS 05137+3919	0.086 ± 0.027	0.201 ± 0.024	-0.12 ± 0.04	-3.18	Hachisuka et al. (2015)
Orion KL	2.39 ± 0.03	2.415 ± 0.040	-0.02 ± 0.05	-0.50	Menten et al. (2007)
IRAS 06058+2138	0.569 ± 0.034	0.476 ± 0.006	0.09 ± 0.03	2.69	Reid et al. (2009a),[†] Sakai et al. (2019)
HH 12-15	1.61 ± 0.36	1.12 ± 0.05	0.48 ± 0.36	1.35	Dzib et al. (2016)
S 255 IR-SMA1	0.563 ± 0.036	0.628 ± 0.027	-0.07 ± 0.04	-1.44	Rygl et al. (2010)
S 269	0.189 ± 0.008	0.241 ± 0.012	-0.05 ± 0.01	-3.61	Quiroga-Nuñez et al. (2019)
VY CMa	0.88 ± 0.08	0.83 ± 0.08	0.05 ± 0.11	0.44	Zhang et al. (2012)
IRAS 07427−2400	0.185 ± 0.027	0.188 ± 0.016	-0.00 ± 0.03	-0.10	Choi et al. (2014)
IRAS 16293−2422	5.6 ± 1.5	7.1 ± 1.3	-1.50 ± 1.98	-0.76	Dzib et al. (2018)
NGC 6334I(N)	0.789 ± 0.161	0.744 ± 0.076	0.05 ± 0.18	0.25	Wu et al. (2014)
G359.62−00.25	0.33 ± 0.14	0.375 ± 0.021	-0.04 ± 0.14	-0.32	Reid et al. (2019)
Sgr B2	0.133 ± 0.038	0.129 ± 0.012	0.00 ± 0.04	0.10	Reid et al. (2009c)
Sgr D	0.423 ± 0.083	0.194 ± 0.161	0.23 ± 0.18	1.26	Reid et al. (2019)
G005.88−00.39	0.78 ± 0.05	0.334 ± 0.020	0.45 ± 0.05	8.28	Sato et al. (2014)
M 17	0.491 ± 0.041	0.505 ± 0.033	-0.01 ± 0.05	-0.27	Xu et al. (2011)
W 48 A	0.433 ± 0.026	0.306 ± 0.045	0.13 ± 0.05	2.44	Zhang et al. (2009)
G048.60+00.02	0.199 ± 0.007	0.093 ± 0.005	0.11 ± 0.01	12.32	Zhang et al. (2013)
G049.19−00.33	0.211 ± 0.016	0.192 ± 0.009	0.02 ± 0.02	1.03	Wu et al. (2014)
IRAS 19213+1723	0.251 ± 0.036	0.162 ± 0.013	0.09 ± 0.04	2.33	Wu et al. (2019)
ON 1	0.404 ± 0.017	0.425 ± 0.036	-0.02 ± 0.04	-0.53	Rygl et al. (2010), Xu et al. (2013)[†]
IRAS 20126+4104	0.750 ± 0.092	0.61 ± 0.02	0.14 ± 0.09	1.49	Moscadelli et al. (2011)
IRAS 20231+3430	0.611 ± 0.022	0.629 ± 0.017	-0.02 ± 0.03	-0.65	Xu et al. (2013)
G097.53+03.18	0.177 ± 0.028	0.133 ± 0.017	0.04 ± 0.03	1.34	Hachisuka et al. (2015)
IRAS 21379+5106	0.262 ± 0.031	0.206 ± 0.007	0.06 ± 0.03	1.76	Choi et al. (2014)
AFGL 2789	0.326 ± 0.031	0.253 ± 0.024	0.07 ± 0.04	1.86	Choi et al. (2014),[†] Sakai et al. (2019)

*If there are multiple references, we refer to these papers (labeled with [†]) that report higher accuracy parallaxes.

results with each other, we employ the astrometric parameters from VLBA/EVN reported in original references with the highest accuracy data for each source rather than those compiled in Reid et al. (2019) because some of their results are the averaged value of multiple VLBI astrometry results. For G359.62−00.25 and Sgr D/G001.14−00.12, we use the parallax values from Reid et al. (2019) because the other references are in preparation.

As seen in the clear correlation in figure 1, most of the astrometry results are consistent within a factor of 1.5 except for a few sources with larger scatter. They are IRAS 05137+3919/G168.06+00.82 (Honma et al. 2011; Hachisuka et al. 2015), Sgr D/G001.14−00.12 (Sakai et al. 2017; Reid et al. 2019),[1] G005.88−00.39 (Motogi et al. 2011; Sato et al. 2014), and G048.60+00.02 (Nagayama et al. 2011a; Zhang et al. 2013). These data show differences larger than a factor of 2.

To compare their differences, we calculate the normalized parallax differences scaled by their joint uncertainties, as defined by the following equation:

$$\Delta\pi/\sigma_{\Delta\pi} \equiv \frac{\pi_{\mathrm{VERA}} - \pi_{\mathrm{VLBA/EVN}}}{\sqrt{\sigma_{\mathrm{VLBA/EVN}}^2 + \sigma_{\mathrm{VLBA/EVN}}^2}}, \qquad (1)$$

in which π_{VERA} and $\pi_{\mathrm{VLBA/EVN}}$ are the parallaxes measured with VERA and VLBA/EVN, respectively, and σ_{VERA} and σ_{VLBA} are the parallax errors for VERA and VLBA/EVN results, respectively. The results are listed in table 2 and the distribution is plotted in figure 2. As seen in figure 2, most of the target sources give consistent results within $\Delta\pi/\sigma_{\Delta\pi} < 3$ or less than a 3σ limit. The first quartile, median, and third quartile are -0.65, 0.35, and 1.49, respectively. The largest discrepant measurements are for G048.60+00.02 (12.32), G005.88−00.39 (8.28), S 269 (−3.61), G135.28+02.80 (−3.43), and IRAS 05137+3919 (−3.18). Sgr D/G001.14−00.12 gives the smaller value of 1.26 due to the exceptionally large relative errors of the

[1] Although it is the largest error bar in the plot, we could not confirm the original reference in Reid et al. (2019).
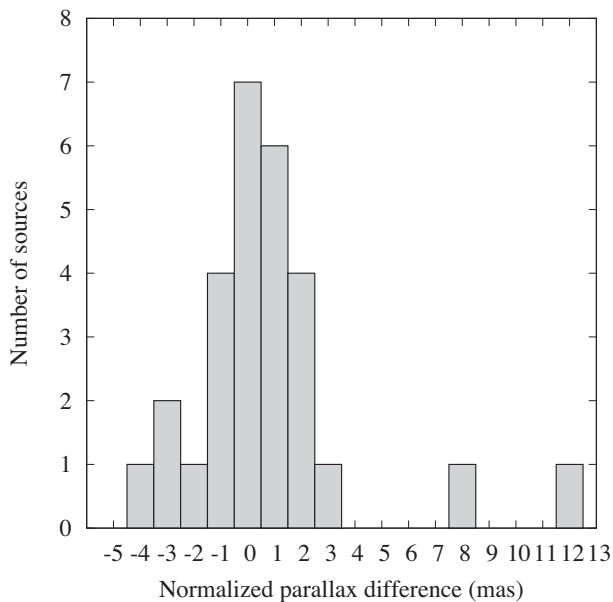
Fig. 2. Histogram of the normalized parallax differences scaled by their joint uncertainties. See definition in equation (1). Each bin has the central value of integer with its width of 1 (e.g., $\Delta\pi/\sigma_{\Delta\pi} = 0.0 \pm 0.5$, 1.0 ± 0.5, -1.0 ± 0.5, ...).

VLBA parallax of $\sim 80\%$. We note that the possible systematic errors in the VERA parallax as discussed in the last paragraph of section 4 are not included in the calculated $\Delta\pi/\sigma_{\Delta\pi}$. Thus, parallax measurements from VERA and VLBA/EVN for 23 out of the total 28 samples (82%) agree with each other within 3σ levels.

Possible origins of such large errors are an insufficient number of observing epochs, in particular around the peak season of the annual parallax value (for IRAS 05137+3919), or errors in the atmospheric calibration and VERA dual-beam phase calibrations (for G048.60+00.02). These results could be improved using additional data and re-calibration processing. Furthermore, spatially extended structures of the target maser features could significantly degrade the accuracy of the position measurement of the maser features, which would introduce additional errors in the astrometry and hence derived parallax values. In fact, the possible effect of such maser structures is intensively discussed for a high-mass YSO S269 at the distance of 4 kpc (Honma et al. 2007; Asaki et al. 2014; Quiroga-Nuñez et al. 2019), in which the possible structure effect results in a parallax error of $> 20\%$. It has been already discussed for the VERA data (Honma et al. 2010) and we revisit this issue in the next sections.

5.2 Comparison for distances toward nearby SFRs

Several astrometry results have been reported for the Orion Molecular Cloud with both VERA and VLBA since the beginning of the VERA and VLBA astrometry projects (Hirota et al. 2007; Kim et al. 2008; Sandstrom et al. 2007; Menten et al. 2007; Kounkel et al. 2017), including the new result from VERA (Nagayama et al. 2020a). In the central part of the Orion region, active high-mass SFRs Orion KL and the Orion Nebular Cluster (ONC) are of the great interest. The VERA results are for observations of the H_2O masers or SiO masers (Orion Source I), while VLBA observes radio continuum emission from different non-thermal radio-emitting YSOs in the ONC region. The first astrometry results for these sources had larger uncertainties of 437 ± 19 pc (Hirota et al. 2007) and 389^{+24}_{-21} pc (Sandstrom et al. 2007) from the VERA H_2O maser and VLBA 15 GHz continuum observations, respectively. Subsequent higher accuracy data of 418 ± 6 pc from the SiO masers with VERA (Kim et al. 2008) and 414 ± 7 pc from the 8 GHz continuum with VLBA (Menten et al. 2007) are in excellent agreement. These results suggest a weighted-mean distance of 416.3 ± 4.6 pc toward the Orion KL region or the central part of the ONC. On the other hand, recent comprehensive studies with VLBA by Kounkel et al. (2017) suggest smaller distances of 388 ± 5 pc as a weighted average of distances of YSOs in the wider area of the ONC.

The possible reason for the differences in these parallax measurements, in particular compared with that of Menten et al. (2007), is discussed in Kounkel et al. (2017); the differences are attributed to the different number of samples, systematic errors originating from ionospheric calibration, multiplicity of the target sources, and/or different treatment of the data for the fitting (e.g., fitting routine for the right ascension and/or declination). If this difference is real, it would suggest the depth of the region along the line-of-sight: Source I could be located in the rear side of the ONC, which argues against Kim et al. (2008).

For other nearby low-mass star-forming regions, we have carried out series of astrometry observations (Imai et al. 2007; Hirota et al. 2007, 2008a, 2008b, 2011; Kim et al. 2008). Similar comprehensive surveys are also carried out by the VLBA large program GOBELINS and their pilot surveys (Loinard et al. 2008; Dzib et al. 2016; Kounkel et al. 2017; Ortiz-León et al. 2017, 2018a). Some of the target regions are common, such as Orion, Monoceros, Ophiuchus, and Perseus molecular clouds. In figure 1, only Orion KL, HH 12-15, and IRAS 16293−2422 in L 1689 are plotted as they are regarded as the same SFRs observed with VERA.

We quantitatively compare the difference in distances between two astrometry measurements. Here we compare distances rather than parallaxes because much of the literature listed mean distances of multiple sources. In the following discussion, the error in the distance difference is calculated from the root sum square of each distance error, and the error in each distance is estimated from the
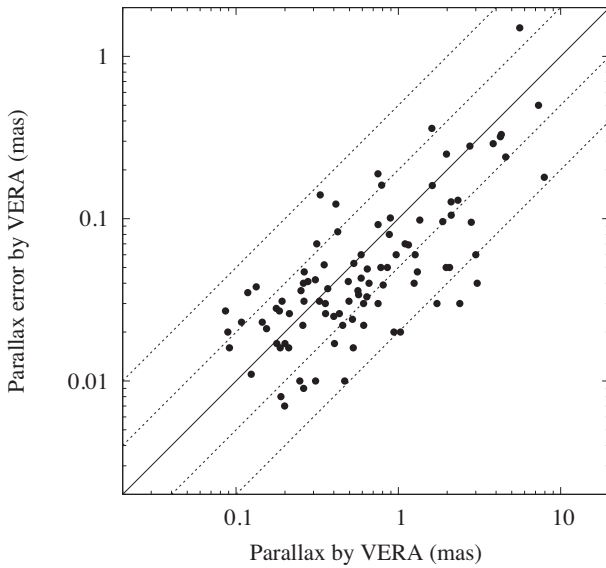
Fig. 3. Parallax values and their errors obtained from the VERA astrometry. A solid line indicates the parallax errors of 10%, while dashed lines represent the errors of 50%, 20%, 5%, and 2%.

geometric mean of both error bars (i.e., $\Delta D = \sqrt{D_1 D_2}$ in a case of $D^{+D_1}_{-D_2}$). The difference between relative errors in the parallax and distance estimated above are as small as $< 0.1\%$–0.3%.

For the Orion regions, GOBELINS also includes various molecular clouds outside Orion KL. One of examples is the L 1641 region at the measured distance of 428 ± 10 pc (Kounkel et al. 2017). The VERA result for another nearby maser source, L 1641 S3, presents the slightly larger distance of 473^{+32}_{-27} pc. The difference in these two distance values of 45 ± 31 pc is not significant with the 1.5σ level. Although VLBA failed to determine the parallax of YSOs in λ Ori possibly due to scattering at the lower frequency (Kounkel et al. 2017), we can measure the parallax of a YSO associated with the λ Ori region, B 35, to be 1.98 ± 0.25 mas in the present paper, corresponding to the distance of 505^{+73}_{-57} pc. The difference in distances between those from GAIA DR2, $402 \pm 1 \pm 20$ pc (Zucker et al. 2019), and VERA is 103 ± 68 pc, which is the 1.5σ level. Because the uncertainty in the parallax value from VERA is still large, future more accurate observations are required to confirm the result.

For YSOs in the Monoceros region, HH (or GGD) 12–15, distances of 620^{+180}_{-110} pc (present paper) from VERA and of 893^{+44}_{-40} pc (Dzib et al. 2016) from VLBA differ by a factor of 45%. The difference in these two distances is -273 ± 147 pc. The error bar of the VERA result, $\sim 20\%$, is relatively larger than the typical value (see figure 3) as discussed in the next subsection.

For the Ophiuchus region, the distances measured by GOBELINS are 137.3 ± 1.2 pc and 147.3 ± 3.4 pc toward dark clouds L 1688 and L 1689, respectively

(Ortiz-León et al. 2017). Parallax measurements for a protostar IRAS 16293−2422, which is located in L 1689, give 178^{+18}_{-37} pc from VERA (Imai et al. 2007) and 141^{+30}_{-21} pc from VLBA (Dzib et al. 2018). These two values from maser astrometry marginally agree with each other (37 ± 36 pc), but the smaller distance of ~ 140 pc is more consistent with those from continuum sources in L 1689.

Compared with the GAIA DR2 results, VLBA results are confirmed to be in good agreement for Ophiuchus (Ortiz-León et al. 2017, 2018b) and Perseus (Ortiz-León et al. 2018a) regions. In the case of another nearby SFR, NGC2264, the distance measured with VERA of 738^{+57}_{-50} pc (Kamezaki et al. 2014a) is in good agreement with the GAIA DR2 value, 719 ± 16 pc (Maíz Apellániz 2019). The mean distance toward slightly farther molecular clouds in Gem OB1, IRAS 06058+2138 (Oh et al. 2010), IRAS 06061+2151 (Niinuma et al. 2011), and S 255 IR-SMA1 (Burns et al. 2016), of 1.85 kpc (with a standard deviation of 0.14 kpc) is also consistent with that from the GAIA DR2 result, $1.786 \pm 0.004 \pm 0.089$ kpc (Zucker et al. 2019). On the other hand, some of the parallax values derived from VERA observations showed significantly large uncertainties which are larger differences than the error bars of VLBA and GAIA results. In the case of the Perseus Molecular Cloud, the VERA results of 234 ± 13 pc from the weighted mean distance of NGC 1333 (Hirota et al. 2008a) and L 1448 (Hirota et al. 2011) is smaller by -59 ± 26 pc than that of GAIA DR2 of 293 ± 22 pc (Ortiz-León et al. 2018a), although the parallax of NGC 1333 was not determined with VLBA alone.

We note that the parallax values of GAIA DR2 would include the zero-point offset with an order of -0.1–0 mas (Gaia Collaboration 2018). More detailed analyses are presented in Xu et al. (2019) and references therein, suggesting that the parallax offset in the GAIA DR2 data is $-75 \pm 29\,\mu$as. It requires the correction of the parallax value corresponding to the systematic uncertainty from -1.5 pc to -180 pc at the distance of 140–1800 pc in the SFRs discussed above. This effect is already considered as the possible systematic error in each reference. In addition, the parallax offset in the GAIA DR2 data would be a more significant effect in the farther target sources. Thus, the large differences in parallax values for nearby SFRs are mostly due to the shorter lifetime of the H_2O masers associated with the low-mass YSOs than the period of annual parallax (i.e., one year), and there seems to be no significant contribution from the zero-point offset in the GAIA DR2 parallaxes. In addition, significant spatial structures of the nearby sources could degrade the accuracy of the position measurements (Imai et al. 2007; Hirota et al. 2008b; Honma et al. 2010; Dzib et al. 2018). We will evaluate this effect in the next section.

5.3 Accuracy and dominant error sources in VERA astrometry

As discussed in Honma et al. (2010), a motion of $0.5 \,\mathrm{km\,s^{-1}}$, which is comparable to typical line widths of the masers (full-width half-maximum of $1 \,\mathrm{km\,s^{-1}}$), corresponds to the transverse distance of 0.1 au within 1 yr. If the motion is systematic, it can partly contribute to the linear proper motion and hence is measurable by the VLBI astrometry monitoring. However, if such a motion originated from turbulence in the maser cloud, it could cause change in the structure of the maser feature randomly. The possible structure change would affect the positional accuracy of the maser features. As a result, this effect will lead to the error in the annual parallax, which is equal to the angular size of 1 au at the distance of the target source, up to 10%. Even larger errors up to 20% or corresponding structure changes of 0.2 au scale would be likely, given the spatially extended nature of maser features (> 1 au).

Figure 3 shows the errors in the parallax as a function of the parallax values. Obviously, the plot shows a clear trend of correlation as seen in the smaller number of samples (Honma et al. 2010). In other word, the errors in the parallaxes are mostly 2%–20% independent of the source distances. It is unlikely that the correlation is mostly due to the calibration errors as they should strongly depend on the separation angles between the calibrators and targets, weather conditions, and source elevation (declination), rather than their distances.

It should be noted that the larger variation in figure 3 than that of Honma et al. (2010) would also reflect different calibration errors and/or method of analysis such as the different number of maser features employed in the parallax fitting and lengths of astrometry monitoring observations. In general, lower declination sources ($\delta < -30°$), such as NGC 6334(I), are more seriously affected by atmospheric calibration errors (Chibueze et al. 2014a). However, we confirm that the correlation of parallaxes and their errors would be the results of source structures.

For the AGB stars, trigonometric parallax measurements can be carried out using the VLBI astrometry of maser sources and optical astrometry like Hipparcos and GAIA (DR2). One example, for the semi-regular variable star SV Peg, demonstrates that there could be significant differences between VLBI and GAIA DR2 astrometry, for which parallax values are 3.00 ± 0.06 mas and 1.12 ± 0.28 mas, respectively (Sudou et al. 2019). The discrepancy is most likely attributable to an effect of unresolved structure of the stellar photosphere observed with GAIA DR2. Xu et al. (2019) discussed the accuracy of parallax measurements of YSOs, AGBs, and pulsars from VLBI astrometry and GAIA DR2, and found the largest differences in the AGB samples. More detailed comparison of astrometry observations

for each AGB star will be discussed in a separate paper (Matsuno et al. 2020; A. Nakagawa et al. in preparation) and hence it is out of the scope of this paper.

The structure effect is thought to be more serious for highly variable sources such as low-mass nearby YSOs and AGB stars (Imai et al. 2007; Hirota et al. 2008b). In contrast, it is demonstrated that astrometry for the compact stellar emission could achieve < 1% parallax accuracy for the nearby open cluster Pleiades (Melis et al. 2014) and continuum sources in the nearby Ophiuchus molecular clouds (Ortiz-León et al. 2017). The structure changes in maser features are found to be less significant for farther (~ 10 kpc) sources because the other error budgets, in particular due to calibration errors of tropospheric delay term (Honma et al. 2008b; Nagayama et al. 2020b), become more significant than those from the source structure. Hence, we note that target maser sources should be selected carefully according to their spatial structures in the synthesized images to overcome this issue. It is also important to make images with better UV coverage to recover both spatially compact and extended emission components. In the case of VERA, lack of shorter baselines (< 1000 km) would seriously resolve out spatially extended maser features. Thus, further KaVA (KVN and VERA Array) and EAVN (East Asian VLBI Network; An et al. 2018) are expected to improve the accuracy of the maser astrometry.

5.4 Galactic structure

The currently available VLBI astrometry results are plotted in figure 4. We plot positions of SFRs and RSGs but
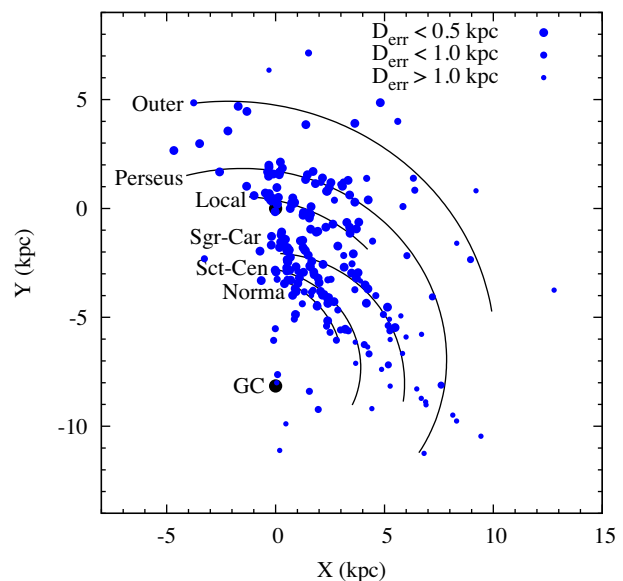

Fig. 4. Distributions of the maser sources on the face-on view of the Galaxy. Solid line show the spiral arm structure identified by the BeSSeL results (Reid et al. 2019).
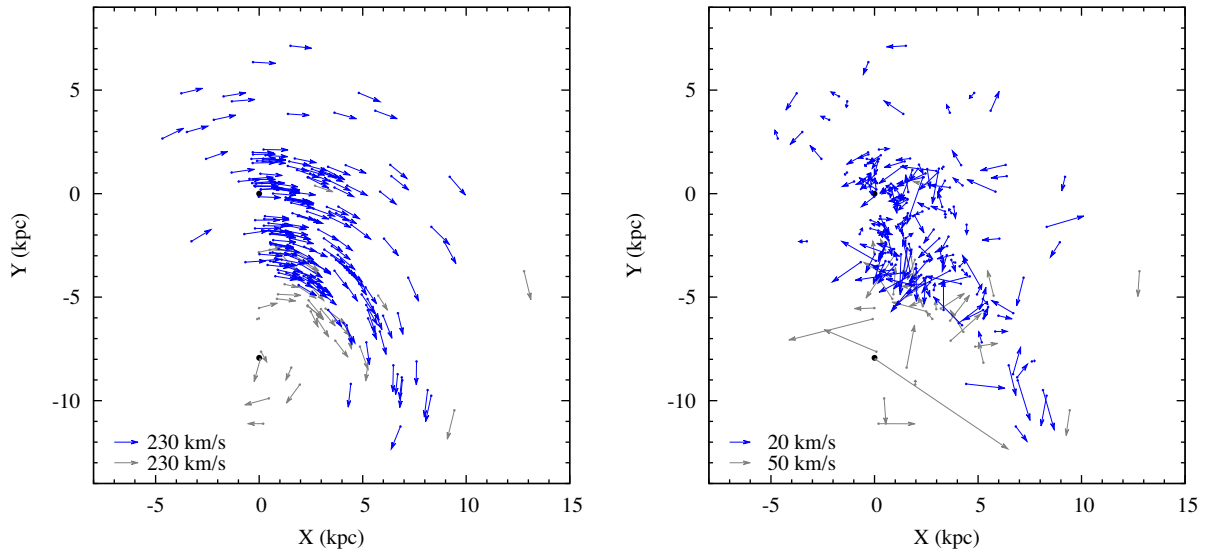
Fig. 5. Galactic rotation motions (left) and peculiar motions (right) of the maser sources. Gray symbols indicate the outliers with $R < 4$ kpc or the peculiar motion of $V > 50$ km s^{-1}, which are removed from the MCMC analysis (see text). The rest of the sources are plotted using blue symbols. The number of blue and gray symbols are 189 and 35, respectively (total: 224 sources). The Galactic parameters for the model with the power-law rotation curve (table 3) and the solar motion of $(U_\odot, V_\odot, W_\odot) = (11.1, 12.24, 7.25)$ in km s^{-1} (Schönrich et al. 2010) are employed to plot the vectors.

AGBs are not included because these sources will not be used for the further analysis, as discussed later. Thus, a total of 224 sources are selected including both VERA and other VLBI results (Reid et al. 2019). We indicate the location of the best-fitted Galactic spiral arms determined by Reid et al. (2019). Most of the target sources are located in the northern hemisphere with the declination of $\delta > -35°$ because of the visibility of the target sources from VERA, VLBA, and EVN. Thus, the sample distribution is strongly biased to the first and second Galactic quadrants ($0° < l < 180°$, where l is the galactic longitude), while less number of sources are located in the third quadrant ($180° < l < 270°$). The only exceptions are two sources, G339.884−1.259 (Krishnan et al. 2015) and G305.2 region (Krishnan et al. 2017), which are observed with the Australian LBA, as plotted in the fourth quadrant ($270° < l < 360°$) of figure 4. The most distant parallax measurement with VLBI is achieved for a high-mass SFR G007.47+00.05 with the trigonometric parallax from the BeSSeL project of 0.049 ± 0.006 mas, corresponding to $20.4^{+2.8}_{-2.2}$ kpc (Sanna et al. 2017). This value is consistent with the astrometry observations with VERA of 20 ± 2 kpc, which is estimated based on the absolute proper motions and radial velocity measurements and three-dimensional Galactic rotation model (Yamauchi et al. 2016).

The Galactic rotation can be seen in figure 5 in which positions of maser sources are plotted with two-dimensional velocity vectors in the Galactic plane. The two-dimensional vectors in the Galactic plane projection

are determined by a combination of sky plane and line-of-sight velocities as mentioned in section 4. To transform from the measurements in a heliocentric frame to the Galacto-centric reference frame, we employ the Galaxy model with the power-law rotation curve as discussed below. The parameters used for the transformation are summarized in table 3. We also assume the solar motion of $(U_\odot, V_\odot, W_\odot) = (11.1, 12.24, 7.25)$ in km s^{-1} (Schönrich et al. 2010). The Galactic rotation curve can be constructed as plotted in figure 6 using the same parameter set. The well-known flat rotation curve is confirmed toward a distance of up to 15 kpc from the Galactic center.

By combining currently available maser astrometry results from VERA, VLBA, EVN, and LBA, we can
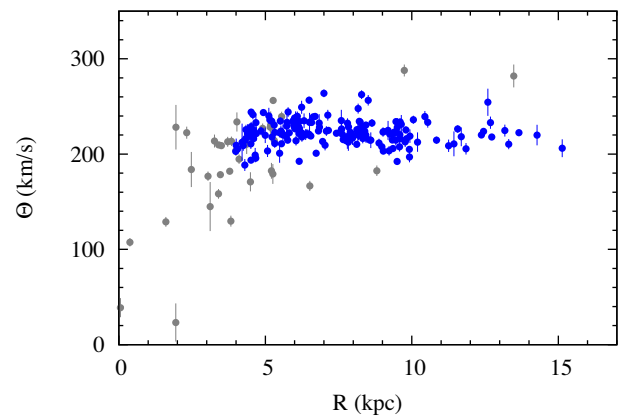

Fig. 6. Rotation curve of the Galaxy. The blue and gray symbols are the same as in figure 5.

Table 3. Estimated Galactic parameters.

Parameter	Power-law model		2nd-order polynomial model	
	Present study	Honma et al. (2012) ID14	Present study	Honma et al. (2012) ID22
R_0 (kpc)	7.92 ± 0.16	7.82 ± 0.41	7.97 ± 0.15	7.70 ± 0.40
Ω_0 (km s^{-1} kpc^{-1})	28.63 ± 0.26	29.60 ± 0.74	28.64 ± 0.26	29.71 ± 0.71
U_s (km s^{-1})	4.2 ± 1.0	0.8 ± 1.4	4.3 ± 1.0	0.7 ± 1.4
V_s (km s^{-1})	-4.9 ± 0.9	-6.3 ± 1.2	-3.7 ± 1.0	-6.5 ± 1.3
W_s (km s^{-1})	-0.4 ± 0.7	-1.9 ± 1.1	-0.4 ± 0.7	-1.9 ± 1.1
α	-0.016 ± 0.012	0.00 ± 0.02	—	—
a_0 (km s^{-1} kpc^{-1})	—	—	-0.5 ± 0.4	-0.1 ± 0.7
b_0 (km s^{-1} kpc^{-2})	—	—	-0.2 ± 0.1	0.1 ± 0.2

estimate the fundamental parameters of the Milky Way Galaxy as discussed in Honma et al. (2012) using an increased number of samples. Here we briefly summarize our data analysis. We employ SFRs and high-mass RSGs but exclude AGB stars for our data analysis. This is because dynamical properties of AGB stars are different from those of former samples, such as velocity dispersion and peculiar motions with respect to the Galactic rotation (known as asymmetric drift). In the model fitting, outliers which have the Galacto-centric distances within < 4 kpc or the peculiar motion of $V > 50$ km s^{-1} are also removed from the input data for further analysis to avoid systematic errors in the estimated parameters. The former condition is considered to exclude systematic motion caused by the Galactic bar (Honma et al. 2012; Reid et al. 2014). These sources are indicated by gray symbols in figures 5 and 6. The number of removed sources is 35, and hence we used a total of 189 sources for the further analysis which are plotted using blue symbols in figures 5 and 6.

In the Galaxy model, we simply assume the circular rotation of the local standard of rest (LSR) with small systematic/random motions. The distance toward the Galactic center and the rotation velocity of the LSR around the Galactic center are referred to as R_0 and Θ_0, respectively. The ratio of Θ_0/R_0 gives the Galactic angular velocity at the LSR, Ω_0. As discussed previously, we will solve a set of R_0 and Ω_0 rather than R_0 and Θ_0, because the latter set is known to be tightly correlated (Reid et al. 2009b; Honma et al. 2012). Although the correlation could become modest due to the increased number of target sources in the larger distribution of our present data, we follow the same data analysis as Honma et al. (2012) to compare the results consistently. For the Galactic rotation curve, we use two different models; a power law, $\Theta(R) = \Theta_0(R/R_0)^\alpha$, and 2nd-order polynomial, $\Theta(R) = \Theta_0 + a_0(R - R_0) + b_0(R - R_0)^2$, functions of rotation curves. The power-law index α or

the polynomial coefficients a_0 and b_0 are also solved in the analysis. In addition, mean systematic motions, (U_s, V_s, and W_s) are introduced in the models to account for the peculiar motions (Reid et al. 2009b; Honma et al. 2012). The U_s, V_s, and W_s are defined as the velocity components toward the Galaxy center, the direction of Galactic rotation, and the north Galactic pole, respectively. The solar motion is assumed to be ($U_\odot$, $V_\odot$, $W_\odot$) = (11.1, 12.24, 7.25) in km s^{-1} (Schönrich et al. 2010).

All the parameters are estimated by the same procedures described in Honma et al. (2012), based on the Markov Chain Monte Carlo (MCMC) method. To explore the posterior probability distribution of the parameters, MCMC simulation is iterated for the trial number of 10^6. Figure 7 shows the posterior probability distribution for six parameters of power-law model. For all parameters, the posterior profitability distribution shows a single-peaked symmetric structure, which confirms reasonable estimates of the parameters. Table 3 summarizes the best parameters and their statistical errors calculated from the means and the standard deviations of the posterior probability distributions in our two Galactic rotation models. As for R_0 and Ω_0, both results agree well with each other with differences less than 1%. These differences are much smaller than the error bars. The inward motion of U_s is non-zero values in contrast to the previous paper (Honma et al. 2012), while the vertical component with respect to the Galactic plane, W_s suggests no significant motion. The power-law index α of -0.016 ± 0.012 is slightly negative but is consistent with the flat rotation curve.

As listed in table 3, we can directly compare the present results with the models of ID 14 for the power-law rotation curve and ID 22 for the polynomial rotation curve (removing outliers and adopting fixed $V_\odot = 12$ km s^{-1}) in Honma et al. (2012). Present results are in good agreement with those in Honma et al. (2012) but the statistical errors
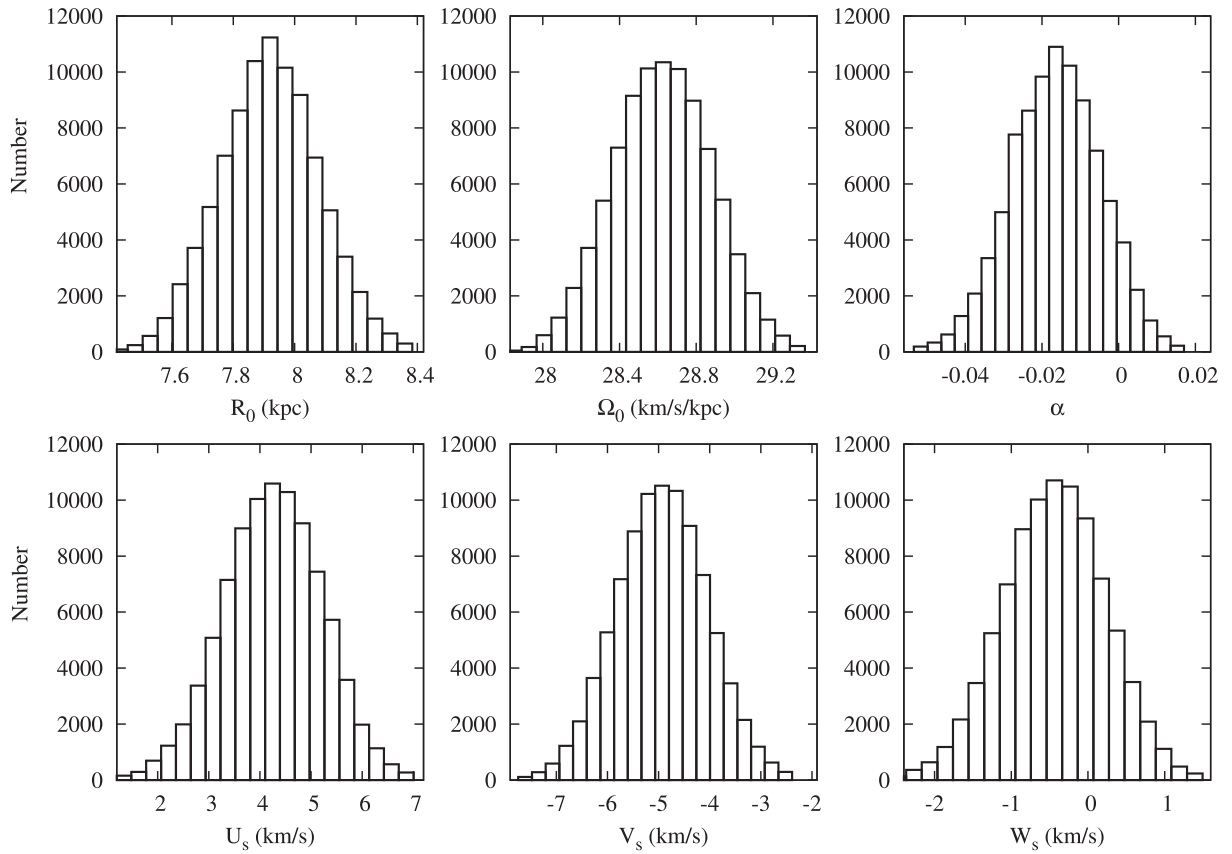
Fig. 7. Posterior probability distribution for the Galactic parameters in the case of the power law model. From top-left to bottom-right, each panel shows a plot for R_0, Ω_0, α, U_s, V_s, and W_s.

for R_0 and Ω_0 estimated by the MCMC method are smaller by a factor of ~ 2.5 as the number of samples increases from 49 to 189. In particular, an increase in the number of future sources would significantly contribute to the improvement of the precision.

As reported in the previous paper (Honma et al. 2012), Ω_0 and $V_\odot$ are tightly correlated and Ω_0 is dependent on the adopted value of $V_\odot$. However, the angular velocity of the Sun defined by $\Omega_\odot \equiv \Omega_0 + V_\odot/R_0$ can be well determined. It is estimated to be $\Omega_\odot = 30.17 \pm 0.27$ km s^{-1} kpc^{-1} using R_0 and Ω_0 in the power-law model shown in table 3 and the adopted value of $V_\odot = 12.24$ km s^{-1} (Schönrich et al. 2010).

As demonstrated in Honma et al. (2012), estimated Galactic fundamental parameters depend on the employed model of the Galaxy and input source samples. In the present paper, we did not perform the MCMC fitting by changing the solar motion. The assumed values of the solar motion would lead to systematic errors in the derived parameters, and hence the uncertainties in the estimated parameters could be underestimated. For instance, the difference in R_0 is as small as <1% while that of Ω_0 is about 6% when $V_\odot$ is assumed to be 5.25 km s^{-1} or 12.0 km s^{-1},

or is solved in the MCMC analysis to be ~ 19 km s^{-1} (table 5 and figure 4 in Honma et al. 2012). The different values of the solar motion also result in the systematic error of Θ_0 of the same magnitude, 6% (table 6 in Honma et al. 2012). However, it does not strongly affect the $\Omega_\odot$ value, which is 0.3% different (table 6 in Honma et al. 2012). In summary, assuming the solar motions in the MCMC analysis would lead to systematic errors of 6% in Ω_0 and Θ_0, while the effect is less than 1% for R_0 and $\Omega_\odot$. In order to take into account the above systematic errors, we estimate a systematic error in R_0 of 4%, adding together the 1% of the model dependency (table 3) and the 3% of the sample dependency (Honma et al. 2015). For the $\Omega_\odot$, the systematic error is 1% mainly due to the sample dependency (Honma et al. 2015), given the smaller differences among models in table 3 (Honma et al. 2012, 2015; Reid et al. 2019).

According to Reid et al. (2019), R_0 and $\Omega_\odot$ are determined to be 8.15 ± 0.15 kpc and 30.32 ± 0.27 km s^{-1} kpc^{-1}, respectively, based on the VLBI astrometry of 147 maser sources, as listed in table 4 and 5. Our results considered that both statistic and systematic errors, $R_0 = 7.92 \pm 0.16_{\text{stat.}} \pm 0.3_{\text{sys.}}$ kpc and $\Omega_\odot = 30.17 \pm 0.27_{\text{stat.}} \pm 0.3_{\text{sys.}}$ km s^{-1} kpc^{-1}, are consistent with

Table 4. Comparison of Galactic center distance R_0.

Method	Reference	R_0 (kpc)
VLBI astrometry of 189 maser sources	Present work	$7.92 \pm 0.16_\text{stat.} \pm 0.3_\text{sys.}$
VLBI astrometry of 147 maser sources	Reid et al. (2019)	8.15 ± 0.15
Orbital motion of S2 around Sgr A*	Gravity Collaboration (2019)	$8.178 \pm 0.013_\text{stat.} \pm 0.022_\text{sys.}$
Orbital motions of S0-2 around Sgr A*	Do et al. (2019)	$7.946 \pm 0.050_\text{stat.} \pm 0.032_\text{sys.}$

Table 5. Comparison of angular velocity of the Sun $\Omega_\odot$.

Method	Reference	$\Omega_\odot$ (km s^{-1} kpc^{-1})
VLBI astrometry of 189 maser sources	Present work	$30.17 \pm 0.27_\text{stat.} \pm 0.3_\text{sys.}$
VLBI astrometry of 147 maser sources	Reid et al. (2019)	30.32 ± 0.27
Proper motion of Sgr A*	Reid and Brunthaler (2020)	30.39 ± 0.04

each other. The small difference in R_0 could be attributed to the Galactic rotation curve employed in the models and/or the different input samples as noted in the previous paragraph (Honma et al. 2012, 2015). As already discussed in previous papers, new VLBI astrometry results are different from those recommended by the International Astronomical Union (IAU), $R_0 = 8.5$ kpc and $\Theta_0 = 220$ km s^{-1} (Kerr & Lynden-Bell 1986). Our results yield $\Theta_0 = R_0\Omega_0 = 227$ km s^{-1}. Thus, R_0 and Θ_0 are smaller by 6% and larger by 3%, respectively. The angular velocity of the Sun, $\Omega_\odot$, is independently determined by proper motion measurements of a supermassive black hole at the Galactic center, Sgr A* (Reid & Brunthaler 2004, 2020). As listed in table 5, all the results of $\Omega_\odot$ are in good agreement. Recently, the distance to Sgr A* was accurately determined to be $R_0 = 8.178 \pm 0.013_\text{stat.} \pm 0.022_\text{sys.}$ kpc (Gravity Collaboration 2019) and $R_0 = 7.946 \pm 0.050_\text{stat.} \pm 0.032_\text{sys.}$ kpc (Do et al. 2019) by measurements of stellar orbital motions around Sgr A* (table 4). Our result is consistent with this. This consistency suggests that Sgr A* is truly located at the dynamical center of the Galactic rotation of the LSR. When we adopt $R_0 = 8.178$ kpc (Gravity Collaboration 2019), the Galactic rotation velocity is $\sim 3\%$ upwardly revised to 234 km s^{-1}.

6 Summary and future prospects

We have compiled all the astrometry measurements from VERA to construct the first version of the VERA catalogue. In total, 99 target sources are listed in the catalogue including 21 new measurements in the present paper. The results are basically consistent with those from other VLBI astrometry projects with VLBA (BeSSeL) and EVN, while significant differences are also reported for several sources. It is mainly affected by the spatial structures of the target maser features and their time variation, along with the systematic calibration errors. The effects are more significant for the nearby lower-mass YSOs and AGBs.

Using the entire available VLBI astrometry data base, we model the Galactic structure to estimate the fundamental parameters such as the distance toward the Galactic center, R_0, the angular velocity of the LSR around the Galactic center, Ω_0, and the model of the rotation curve. Using these parameters, the angular velocity of the Sun, $\Omega_\odot$, is calculated for comparison with the other results. The results, $R_0 = 7.92 \pm 0.16_\text{stat.} \pm 0.3_\text{sys.}$ kpc and $\Omega_\odot = 30.17 \pm 0.27_\text{stat.} \pm 0.3_\text{sys.}$ km s^{-1} kpc^{-1} are also consistent with those from VLBA (Reid et al. 2019).

Further astrometry observations with VERA will be able to advance the studies on the Galaxy model by increasing the number of target sources along with reducing systematic errors due to insufficient samples (Honma et al. 2015). New VLBI arrays such as KaVA/EAVN and those in southern hemisphere, LBA (Krishnan et al. 2015, 2017) and the future SKA (Square Kilometer Array) in the VLBI mode (Green et al. 2015) will improve astrometry accuracy for spatially extended sources and southern sources, respectively, which are still insufficient for the currently available VERA catalogue. The new data analysis tool, VEDA, will provide systematic astrometry results for future VERA observational data and reanalysis of previous archive data (Nagayama et al. 2020a).

Supplementary data

The following supplementary data is available at PASJ online.

ASCII format data of table 1.

Acknowledgment

References

An, T., Sohn, B. W., & Imai, H. 2018, Nature Astron., 2, 118

Ando, K., et al. 2011, PASJ, 63, 45

Asaki, Y., Imai, H., Sobolev, A. M., & Parfenov, S. Yu. 2014, ApJ, 787, 54

Beasley, A. J., Gordon, D., Peck, A. B., Petrov, L., MacMillan, D. S., Fomalont, E. B., & Ma, C. 2002, ApJS, 141, 13

Burns, R. A., et al. 2014a, PASJ, 66, 102

Burns, R. A., et al. 2017, MNRAS, 467, 2367

Burns, R. A., Handa, T., Nagayama, T., Sunada, K., & Omodaka, T. 2016, MNRAS, 460, 283

Burns, R. A., Imai, H., Handa, T., Omodaka, T., Nakagawa, A., Nagayama, T., & Ueno, Y. 2015, MNRAS, 453, 3163

Burns, R. A., Nagayama, T., Handa, T., Omodaka, T., Nakagawa, A., Nakanishi, H., Hayashi, M., & Shizugami, M. 2014b, ApJ, 797, 39

Chibueze, J. O., et al. 2014a, ApJ, 784, 114

Chibueze, J. O., et al. 2014b, PASJ, 66, 104

Chibueze, J. O., et al. 2016, MNRAS, 460, 1839

Chibueze, J. O., et al. 2019, PASJ, 71, 92

Chibueze, J. O., et al. 2020, PASJ, 72, 54

Chibueze, J. O., Hamabata, H., Nagayama, T., Omodaka, T., Handa, T., Sunada, K., Nakano, M., & Ueno, Y. 2017, MNRAS, 466, 4530

Chikada, Y., Kawaguchi, N., Inoue, M., Morimoto, M., Kobayashi, H., & Mattori, S. 1991, in Frontiers of VLBI, ed. H. Hirabayashi et al. (Tokyo: Universal Academy Press), 79

Choi, Y. K., et al. 2008, PASJ, 60, 1007

Choi, Y. K., Hachisuka, K., Reid, M. J., Xu, Y., Brunthaler, A., Menten, K. M., & Dame, T. M. 2014, ApJ, 790, 99

Do, T., et al. 2019, Science, 365, 664

Dzib, S. A., et al. 2018, A&A, 614, A20

Dzib, S. A., Ortiz-León, G. N., Loinard, L., Mioduszewski, A. J., Rodríguez, L. F., Torres, R. M., & Deller, A. 2016, ApJ, 826, 201

Gaia Collaboration 2018, A&A, 616, A1

Gravity Collaboration 2019, A&A, 625, L10

Green, J., Van Langevelde, H. J., Brunthaler, A., Ellingsen, S., Imai, H., Vlemmings, W., Reid, M., & Richards, A. 2015, in PoS (AASKA14), Advancing Astrophysics with the Square Kilometre Array, ed. T. L. Bourke et al. (Trieste: SISSA), 119

Hachisuka, K., et al. 2006, ApJ, 645, 337

Hachisuka, K., Brunthaler, A., Menten, K. M., Reid, M. J., Hagiwara, Y., & Mochizuki, N. 2009, ApJ, 696, 1981

Hachisuka, K., Choi, Y. K., Reid, M. J., Brunthaler, A., Menten, K. M., Sanna, A., & Dame, T. M. 2015, ApJ, 800, 2

Hirota, T., et al. 2007, PASJ, 59, 897

Hirota, T., et al. 2008a, PASJ, 60, 37

Hirota, T., et al. 2008b, PASJ, 60, 961

Hirota, T., Honma, M., Imai, H., Sunada, K., Ueno, Y., Kobayashi, H., & Kawaguchi, N. 2011, PASJ, 63, 1

Honma, M., et al. 2007, PASJ, 59, 889

Honma, M., et al. 2008a, PASJ, 60, 935

Honma, M., et al. 2010, Publ. Natl. Astron. Obs. Jpn., 13, 57

Honma, M., et al. 2012, PASJ, 64, 136

Honma, M., Hirota, T., Kan-Ya, Y., Kawaguchi, N., Kobayashi, H., Kurayama, T., & Sato, K. 2011, PASJ, 63, 17

Honma, M., Nagayama, T., & Sakai, N. 2015, PASJ, 67, 70

Honma, M., Tamura, Y., & Reid, M. J. 2008b, PASJ, 60, 951

Iguchi, S., Kurayama, T., Kawaguchi, N., & Kawakami, K. 2005, PASJ, 57, 259

Imai, H., et al. 2007, PASJ, 59, 1107

Imai, H., Kurayama, T., Honma, M., & Miyaji, T. 2013, PASJ, 65, 28

Imai, H., Sakai, N., Nakanishi, H., Sakanoue, H., Honma, M., & Miyaji, T. 2012, PASJ, 64, 142

Imai, H., Tafoya, D., Honma, M., Hirota, T., & Miyaji, T. 2011, PASJ, 63, 81

Iwata, Y., Kato, H., Sakai, D., & Oka, T. 2017, ApJ, 840, 18

Jike, T., Manabe, S., & Tamura, Y. 2009, J. Geodetic Soc. Jpn., 55, 369

Jike, T., Manabe, S., & Tamura, Y. 2018, J. Geodetic Soc. Jpn., 63, 193

Kamezaki, T., et al. 2012, PASJ, 64, 7

Kamezaki, T., et al. 2014a, ApJS, 211, 18

Kamezaki, T., et al. 2016a, PASJ, 68, 71

Kamezaki, T., Kurayama, T., Nakagawa, A., Handa, T., Omodaka, T., Nagayama, T., Kobayashi, H., & Shizugami, M. 2014b, PASJ, 66, 107

Kamezaki, T., Nakagawa, A., Omodaka, T., Inoue, K., Chibueze, J. O., Nagayama, T., Ueno, Y., & Matsunaga, N. 2016b, PASJ, 68, 75

Kamohara, R., et al. 2010, A&A, 510, A69

Kerr, F. J., & Lynden-Bell, D. 1986, MNRAS, 221, 1023

Kim, M. K., et al. 2008, PASJ, 60, 991

Koide, N., et al. 2019, PASJ, 71, 113

Kounkel, M., et al. 2017, ApJ, 834, 142

Kovalevsky, J. 1998, ARA&A, 36, 99

Krishnan, V., et al. 2015, ApJ, 805, 129

Krishnan, V., Ellingsen, S. P., Reid, M. J., Bignall, H. E., McCallum, J., Phillips, C. J., Reynolds, C., & Stevens, J. 2017, MNRAS, 465, 1095

Kurayama, T., Nakagawa, A., Sawada-Satoh, S., Sato, K., Honma, M., Sunada, K., Hirota, T., & Imai, H. 2011, PASJ, 63, 513

Kusuno, K., Asaki, Y., Imai, H., & Oyama, T. 2013, ApJ, 774, 107

Loinard, L., Torres, R. M., Mioduszewski, A. J., & Rodríguez, L. F. 2008, ApJ, 675, L29

Maíz Apellániz, J. 2019, A&A, 630, A119

Manabe, S., Yokoyama, K., & Sakai, S. 1991, IERS Technical Note, 8, 61

Matsumoto, N., et al. 2011, PASJ, 63, 1345

Matsuno, M., et al. 2020, PASJ, 72, 56

Melis, C., Reid, M. J., Mioduszewski, A. J., Stauffer, J. R., & Bower, G. C. 2014, Science, 345, 1029

Menten, K. M., Reid, M. J., Forbrich, J., & Brunthaler, A. 2007, A&A, 474, 515

Min, C., Matsumoto, N., Kim, M. K., Hirota, T., Shibata, K. M., Cho, S.-H., Shizugami, M., & Honma, M. 2014, PASJ, 66, 38

Moscadelli, L., Cesaroni, R., Rioja, M. J., Dodson, R., & Reid, M. J. 2011, A&A, 526, A66

Motogi, K., et al. 2016, PASJ, 68, 69

Motogi, K., Sorai, K., Habe, A., Honma, M., Kobayashi, H., & Sato, K. 2011, PASJ, 63, 31

Müller, H. S. P., Thorwirth, S., Roth, D. A., & Winnewisser, G. 2001, A&A, 370, L49

Nagayama, T., et al. 2015a, PASJ, 67, 65

Nagayama, T., et al. 2015b, PASJ, 67, 66

Nagayama, T., et al. 2020a, PASJ, 72, 51

Nagayama, T., et al. 2020b, PASJ, 72, 52

Nagayama, T., Omodaka, T., Handa, T., Honma, M., Kobayashi, H., Kawaguchi, N., & Ueno, Y. 2011a, PASJ, 63, 719

Nagayama, T., Omodaka, T., Nakagawa, A., Handa, T., Honma, M., Kobayashi, H., Kawaguchi, N., & Miyaji, T. 2011b, PASJ, 63, 23

Nakagawa, A., et al. 2008, PASJ, 60, 1013

Nakagawa, A., et al. 2014, PASJ, 66, 101

Nakagawa, A., Kurayama, T., Matsui, M., Omodaka, T., Honma, M., Shibata, K. M., Sato, K., & Jike, T. 2016, PASJ, 68, 78

Nakanishi, H., et al. 2015, PASJ, 67, 68

Niinuma, K., et al. 2011, PASJ, 63, 9

Nyu, D., et al. 2011, PASJ, 63, 63

Ogbodo, C. S., et al. 2017, MNRAS, 469, 4788

Oh, C. S., Kobayashi, H., Honma, M., Hirota, T., Sato, K., & Ueno, Y. 2010, PASJ, 62, 101

Omodaka, T., et al. 2020, PASJ, 72, 55

Ortiz-León, G. N., et al. 2017, ApJ, 834, 141

Ortiz-León, G. N., et al. 2018a, ApJ, 865, 73

Ortiz-León, G. N., et al. 2018b, ApJ, 869, L33

Oyama, T., et al. 2016, PASJ, 68, 105

Petrov, L., Honma, M., & Shibata, S. M. 2012, AJ, 143, 35

Petrov, L., Hirota, T., Honma, M., Shibata, K. M., Jike, T., & Kobayashi, H. 2007, AJ, 133, 2487

Pickett, H. M., Poynter, R. L., Cohen, E. A., Delitsky, M. L., Pearson, J. C., & Müller, H. S. P. 1998, J. Quant. Spectrosc. Radiat. Transfer, 60, 883

Quiroga-Nuñez, L. H., Immer, K., van Langevelde, H. J., Reid, M. J., & Burns, R. A. 2019, A&A, 625, A70

Reid, M. J., et al. 2009b, ApJ, 700, 137

Reid, M. J., et al. 2014, ApJ, 783, 130

Reid, M. J., et al. 2019, ApJ, 885, 131

Reid, M. J., & Brunthaler, A. 2004, ApJ, 616, 872

Reid, M. J., & Brunthaler, A. 2020, ApJ, 892, 39

Reid, M. J., & Honma, M. 2014, ARA&A, 52, 339

Reid, M. J., Menten, K. M., Brunthaler, A., Zheng, X. W., Moscadelli, L., & Xu, Y. 2009a, ApJ, 693, 397

Reid, M. J., Menten, K. M., Zheng, X. W., Brunthaler, A., & Xu, Y. 2009c, ApJ, 705, 1548

Reid, M. J., Schneps, M. H., Moran, J. M., Gwinn, C. R., Genzel, R., Downes, D., & Roennaeng, B. 1988, ApJ, 330, 809

Rygl, K. L. J., Brunthaler, A., Reid, M. J., Menten, K. M., van Langevelde, H. J., & Xu, Y. 2010, A&A, 511, A2

Sakai, D., Oyama, T., Nagayama, T., Honma, M., & Kobayashi, H. 2017, PASJ, 69, 64

Sakai, N., et al. 2015, PASJ, 67, 69

Sakai, N., et al. 2020, PASJ, 72, 53

Sakai, N., Honma, M., Nakanishi, H., Sakanoue, H., Kurayama, T., Shibata, K. M., & Shizugami, M. 2012, PASJ, 64, 108

Sakai, N., Reid, M. J., Menten, K. M., Brunthaler, A., & Dame, T. M. 2019, ApJ, 876, 30

Sakai, N., Sato, M., Motogi, K., Nagayama, T., Shibata, K. M., Kanaguchi, M., & Honma, M. 2014, PASJ, 66, 3

Sandstrom, K. M., Peek, J. E. G., Bower, G. C., Bolatto, A. D., & Plambeck, R. L. 2007, ApJ, 667, 1161

Sanna, A., Reid, M. J., Dame, T. M., Menten, K. M., & Brunthaler, A. 2017, Science, 358, 227

Sato, M., et al. 2008, PASJ, 60, 975

Sato, M., et al. 2014, ApJ, 793, 72

Sato, M., Hirota, T., Reid, M. J., Honma, M., Kobayashi, H., Iwadate, K., Miyaji, T., & Shibata, K. M. 2010, PASJ, 62, 287

Schönrich, R., Binney, J., & Dehnen, W. 2010, MNRAS, 403, 1829

Shiozaki, S., Imai, H., Tafoya, D., Omodaka, T., Hirota, T., Honma, M., Matsui, M., & Ueno, Y. 2011, PASJ, 63, 1219

Sudou, H., et al. 2019, PASJ, 71, 16

Tafoya, D., et al. 2011, PASJ, 63, 71

Ulich, B. L., & Haas, R. W. 1976, ApJS, 30, 247

Urago, R., et al. 2020, PASJ, 72, 57

Wu, Y. W., et al. 2014, A&A, 566, A17

Wu, Y. W., et al. 2019, ApJ, 874, 94

Xu, S., Zhang, B., Reid, M. J., Zheng, X., & Wang, G. 2019, ApJ, 875, 114

Xu, Y., et al. 2013, ApJ, 769, 15

Xu, Y., Moscadelli, L., Reid, M. J., Menten, K. M., Zhang, B., Zheng, X. W., & Brunthaler, A. 2011, ApJ, 733, 25

Xu, Y., Reid, M. J., Zheng, X. W., & Menten, K. M. 2006, Science, 311, 54

Yamauchi, A., Yamashita, K., Honma, M., Sunada, K., Nakagawa, A., & Ueno, Y. 2016, PASJ, 68, 60

Zhang, B., Reid, M. J., Menten, K. M., & Zheng, X. W. 2012, ApJ, 744, 23

Zhang, B., Reid, M. J., Menten, K. M., Zheng, X. W., Brunthaler, A., Dame, T. M., & Xu, Y. 2013, ApJ, 775, 79

Zhang, B., Zheng, X. W., Reid, M. J., Menten, K. M., Xu, Y., Moscadelli, L., & Brunthaler, A. 2009, ApJ, 693, 419

Zucker, C., Speagle, J. S., Schlafly, E. F., Green, G. M., Finkbeiner, D. P., Goodman, A. A., & Alves, J. 2019, ApJ, 879, 125